WL-TR-96-4016

CERAMIC BEARING DEVELOPMENT

VOL 2, DEVELOPMENT OF SURFACE ACOUSTIC WAVE
NDE FOR SILICON NITRIDE BALLS

CHUNG-KAO PETER HSEIH, PH.D.
BUTRUS T. KHURI-YAKUB, PH.D.
CHARLES BURK

NORTON ADVANCED CERAMICS
DIVISION OF SGNICC
10 AIRPORT PARK ROAD
EAST GRANBY, CT   06026

MARCH 1995

INTERIM REPORT FOR 07/01/92-10/01/94

APPROVED FOR PUBLIC RELEASE; DISTRIBUTION IS UNLIMITED.

19961031 046

MATERIALS DIRECTORATE
WRIGHT LABORATORY
AIR FORCE MATERIEL COMMAND
WRIGHT PATTERSON AFB OH 45433-7734

NOTICE

When government drawings, specifications, or other data are used for any purpose other than in connection with a definitely related government procurement operation, the United States Government thereby incurs no responsibility nor any obligation whatsoever; and the fact that the government may have formulated, furnished, or in any way supplied the said drawings, specifications, or other data, is not to be regarded by implication or otherwise as in any manner licensing the holder or any other person or corporation, or conveying any rights or permission to manufacture, use, or sell any patented invention that may in any way be related thereto.

This report is releasable to the National Technical Information Service (NTIS). At NTIS, it will be available to the general public, including foreign nations.

This technical report has been reviewed and is approved for publication.

KARL R. MECKLENBURG, Project Engineer
Nonstructural Materials Branch
Nonmetallic Materials Division

KENT J. EISENTRAUT, Chief
Nonstructural Materials Branch
Nonmetallic Materials Division

CHARLES E. BROWNING, Chief
Nonmetallic Materials Division
Materials Directorate

If your address has changed, if you wish to be removed from our mailing list, or if the addressee is no longer employed by your organization, please notify WL/MLBT, Bldg 654, 2941 P Street, Suite 1, Wright-Patterson AFB OH 45433-7750 to help maintain a current mailing list.

Copies of this report should not be returned unless return is required by security considerations, contractual obligations, or notice on a specific document.

1. AGENCY USE ONLY (Leave blank)	2. REPORT DATE MAR 1995	3. REPORT TYPE AND DATES COVERED INTERIM 07/01/92--10/01/94

4. TITLE AND SUBTITLE CERAMIC BEARING DEVELOPMENT

VOL 2, DEVELOPMENT OF SURFACE ACOUSTIC WAVE NDE FOR SILICON NITRIDE BALLS

5. FUNDING NUMBERS
C F33615-92-C-5917
PE 62712
PR 8355
TA 00
WU 07

6. AUTHOR(S)
CHUNG-KAO PETER HSEIH, PH.D.
BUTRUS T. KHURI-YAKUB, PH.D.
CHARLES BURK

7. PERFORMING ORGANIZATION NAME(S) AND ADDRESS(ES)

NORTON ADVANCED CERAMICS
DIV OF SGNICC
10 AIRPORT PARK RD
EAST GRANBY CT 06026

8. PERFORMING ORGANIZATION REPORT NUMBER

9. SPONSORING/MONITORING AGENCY NAME(S) AND ADDRESS(ES)

MATERIALS DIRECTORATE
WRIGHT LABORATORY
AIR FORCE MATERIEL COMMAND
WRIGHT PATTERSON AFB OH 45433-7734

10. SPONSORING/MONITORING AGENCY REPORT NUMBER

WL-TR-96-4016

11. SUPPLEMENTARY NOTES

12a. DISTRIBUTION/AVAILABILITY STATEMENT

APPROVED FOR PUBLIC RELEASE; DISTRIBUTION IS UNLIMITED.

12b. DISTRIBUTION CODE

13. ABSTRACT (Maximum 200 words)

The Major Objective of the Development of a Surface Acoustic Wave Nondestructive Evaluation (NDE) Technique for Silicon Nitride Balls was to improve hybrid bearing reliability by the elimination of critical size flaws that cause early failures.

A Surface Acoustic Wave NDE technique was developed for Norton Advanced Ceramics NBD-200 silicon nitride balls. System performance was verified on balls with both natural and artificial flaws. A production lot of NBD-200 balls was tested using this method. The production lot was sorted for fatigue testing at 2.9 MPa (420 KSI) contact stress at The Timken Co.

Results suggest that the technique can readily identify certain life limiting flaws. However, fatigue testing of balls inspected with this technique showed no improvement in reliability.

14. SUBJECT TERMS
Surface Acoustic Wave Non Destructive Evaluation
Laser Ultrasound   One Point Contact Measurement
Bearing Ball Testing

15. NUMBER OF PAGES
61

16. PRICE CODE

17. SECURITY CLASSIFICATION OF REPORT UNCLASSIFIED	18. SECURITY CLASSIFICATION OF THIS PAGE UNCLASSIFIED	19. SECURITY CLASSIFICATION OF ABSTRACT UNCLASSIFIED	20. LIMITATION OF ABSTRACT SAR

i

Table of Contents

List of Figures

List of Figures (Continued)

List of Figures (Continued)

List of Tables

FOREWORD

This work was performed by Stanford University, in co-operation with, and as a subcontractor to, Norton Advanced Ceramics Division of Saint Gobain/Norton Industrial Ceramics Corporation. This report presents the results of two main tasks included in Subcontract No. 2885 of Prime Contract F33615-92-C-5917, issued by the United States Department of the Air Force, Air Force Systems Command, WPAFB, OH.

This written report is mainly the work of Butrus T. Khuri-Yakub, Ph.D., in cooperation with, and as a subcontractor to, Norton Advanced Ceramics Division of Saint Gobain/Norton Industrial Ceramics Corporation. The contributing effort of Chung-Kao Peter Hseih, Ph.D., for writing the Appendix, "Laser Ultrasound: One-Point-Contact Measurement", key to the success of this program, is gratefully acknowledged.

The work described herein is specific to Norton Advanced Ceramics NBD-200 material and may not represent the capabilities of other silicon nitride materials.

Several additions, changes and edits were made to this report at Norton Advanced Ceramics.

1.0 SUMMARY

This report presents the work accomplished under Contract F33615-92-C-5917: Subcontract 2885, awarded to Stanford University, for the development of an NDE technique for silicon nitride balls. The major objective of this work was to improve hybrid bearing bearing reliability by the elimination of critical size flaws that cause early failures.

Two main tasks were included in this Subcontract. These were: develop and demonstrate a Surface Acoustic Wave NDE technique for NBD-200 silicon nitride balls, and verification of this technique as an NDE inspection method by fatigue life testing of balls inspected using this technique.

A single point contact Surface Acoustic Wave Inspection technique was developed. This technique was demonstrated on balls containing both natural and artificial defects, with some success. A theoretical model was developed for the system and predicted results were compared to experimental results.

A quantity of 250 7/16" NBD-200 balls were inspected using the technique developed. Of these 250 balls, 224 were tested in hybrid bearings, at 2.9 MPa (420 KSI) contact stress.

Post-mortem analysis of failures in the hybrid bearing tests were conducted. These results have been discussed in more detail in Volume One of this report.

The technique was not entirely successful in improving reliability, but did show some promise for identification of specific defect types in silicon nitride balls.

1

2.0 INTRODUCTION

Silicon nitride bearing balls hold a great deal of promise for replacing steel bearing balls in a number of critical applications. However, ceramics are brittle materials, and the presence of surface and near surface defects, such as inclusions or cracks in the bearing balls, are very detrimental to their performance. Thus, there is a great need for a reliable, quantitatve, NDE technique for silicon nitride bearing balls. The Tasks of this Subcontract that support this need are outlined below:

Task 3.1.1 Characterize Defects in NBD-200 Bearing Balls

  Natural Defects

  Artificial Defects

Task 3.1.5 Develop Non-Contact Acoustic NDE Method

  Develop Excitation and Picʰup Techniques

  Develop Theoretical Model

  Inspect Balls With Natural and Artificial Defects

  Task 3.1.6 NDE and Life Test of Balls

Tasks 3.1.1 and 3.1.5 were combined in this report. Details of the Non-Contact Acoustic Technique have been furnished in the Appendix.

3.0 DEVELOPMENT OF NON-CONTACT ACOUSTIC NDE METHOD: TASK 3.1.5s

3.1 Development of Excitation and Pickup Technique

Prior to the work on this contract, a two point contact resonant sphere technique had been developed and used experimentally for surface defect inspection of silicon nitride balls. This method had several practical limitations when used to inspect small spheres. An improved Single Point Contact Surface Acoustic Wave technique was developed to overcome these limitations.

The concept for this inspection method is shown in Figure 1. A driven transducer excites longitudinal plane waves in a fused quartz buffer rod. The test ball rests on one contact point in the bottom of a precise spherical depression in the the rod. The precise radius promotes coupling efficiency. The buffer rod drives the ball, producing surface wave resonances in the ball. The displacements caused by the surface waves are measured by a laser heterodyne interferometer at the "north pole" of the ball.

The major advantage of this technique is that the ball is contacted only at one point. The size of the contact area is determined by the size of the ball and its mechanical properties. Another advantage is that the frequency of operation can range from DC to 100's of megahertz. This is important when investigating the excitation and detection of resonant modes corresponding to shear, torsional and surface acoustic waves, because different modes are sensitive to different properties and defects in the balls.

The premise of this technique is that by measuring the low frequency resonance (shear and torsional waves) one measures the mechanical properties of the ball, while measuring the high frequency resonance (surface waves) one measures the presence of surface and near surface defects in the balls. This technique is the only known technique that can non-destructively excite and detect high frequency surface waves on balls.

A full description of the system and some sample results are presented in the Appendix which is a portion of a PhD Thesis.

SURFACE ACOUSTIC WAVE INSPECTION
SINGLE POINT CONTACT TECHNIQUE

- LASER INTERFEROMETER (Amplitude & Phase)
- FOCUSING LENS
- LASER BEAM
- TEST BALL
- BUFFER ROD
- TRANSDUCER
- EXCITER
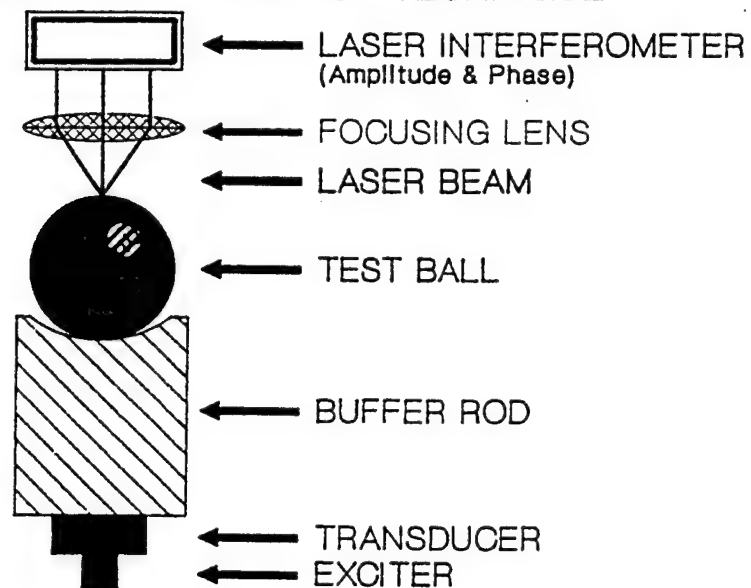
Figure 1: Single Point Contact Surface Acoustic Wave Inspection Technique.

4

3.2 Development of Theoretical Model

The resonant frequencies of a solid sphere, which is an inherent resonant system for surface waves diverging and converging periodically on its free surface, are given by the solutions of a transcendental equation. The equation is obtained by imposing the boundary conditions of zero traction at the free surface as well as the continuity conditions of the various eigenfunctions. The amplitude distribution on the surface is given by the Legendre function $P_n(\cos\theta)$ of order n and, along the radius, by spherical Bessel functions and their derivatives, $j^n(kr)$ and $j'_n(kr)$, where θ is the polar angle coordinate, r is the radial coordinate, and prime indicates differentiation with respect to the argument. For a given integer n, the lowest solution corresponds to Rayleigh waves, the higher ones are referred to as "whispering gallery'' waves. This seems to be a general feature of waves propagating in a curved free surface, i.e., they can be grouped into Rayleigh waves and whispering gallery waves. The penetration depths of the diverse modes are different. Thus, an appropriate mode and order may be chosen to emphasize a region of interest. The resonance of Rayleigh waves and the first two modes of whispering gallery waves were examined in this study. For good balls, the observed resonant frequencies were in agreement with the theory. The degree of badness could be correlated with the deviation of the resonant frequencies from the theoretical predictions.

The spectrum of a solid ceramic sphere is shown in Figure 2. The normalized frequency is given by $\omega a/v_t$, where ω is the circular frequency, a is the radius of the ball, and v_t is the transverse shear velocity. Figure 3 presents the behavior of the first five modes for high frequency. These values have been calculated for Poisson's ratio, $\nu = .262$, corresponding to a measured value from an earlier experiment. The lowest branch, for $n \geq 1$, corresponds to Rayleigh waves, and the higher ones to the so-called "whispering gallery" waves. When n tends to infinity, the Rayleigh wave tends to ordinary Rayleigh waves propagating on a plane surface. We note that $(n+1)2\pi$ corresponds to the phase shift for waves propagating one revolution, $2\pi a$, around the sphere; thus increasing n is equivalent to increasing ka. When n is small, the curvature of the surface plays an important role.

All of the whispering gallery modes start from n=1 at

5

various frequencies. However, the second, fourth, . . .
whispering gallery waves, which correspond to the longitudinal
wave radial resonance, start at n=0. We note that for n=0, the
first, third, . . . whispering gallery waves, correspond to
imaginary shear wave radial resonance, which do not exist
physically. For each whispering gallery mode or Rayleigh mode,
every integer n value refers to a resonant frequency of order n.
We recall that the angular distribution of vibration is given by
$P_n(\cos\theta)$. Thus the feature of the normal displacement on a free
solid surface is similar to that of a gas bubble in water.

It was also shown that the resonant frequency of the lowest
branch approaches $f=nv_R/(2\pi a)$, as n becomes large, where v_R
denotes Rayleigh wave velocity. The penetration depth of the
Rayleigh branch is approximately $1.5\lambda_R$ where λ_R is Rayleigh's
wavelength defined by $\lambda_R=2\pi v_R/\omega$. We also found that the
whispering gallery branches become nondispersive as n becomes
large and that their resonant frequency can be written as
$f=cnv_t/2\pi a$, where c is a numerical factor that depends on the
branch number.
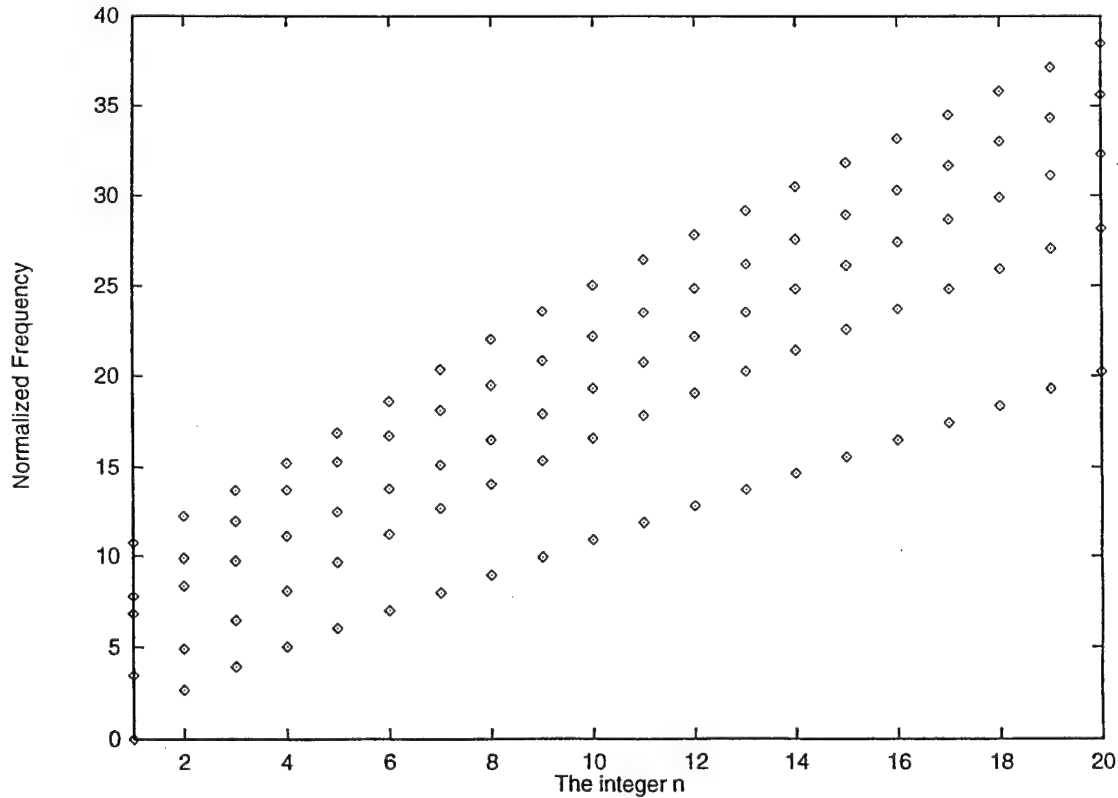
Figure 2: Spectrum of a Ceramic Sphere

6
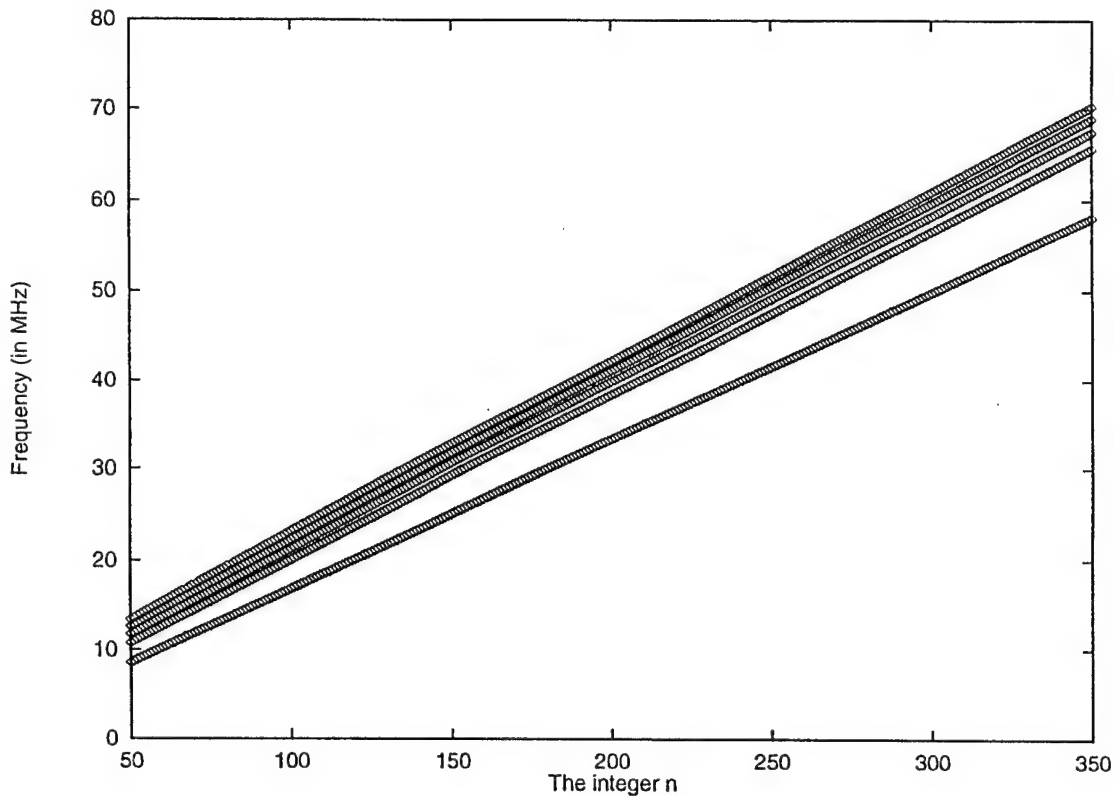
Figure 3: Theoretical Resonances

3.3 Inspection of Balls with Natural and Artificial Defects

Initial tests were made on 50 balls, some that passed all Cerbec inspections with no defects, some with natural defects, and some with different types of artificial defects. The natural defects were iron rich regions, low density regions, large points of out of roundness, and long meandering scratches. The artificial defects were Vickers indentation cracks of various sizes. These artificial cracks were similar in size to those used in the baseline life testing performed at Timken Research and the thermal proof testing at University of Dayton. All these samples were inspected using this acoustic NDE technique. The defective balls were easy to identify by the defects' influence on surface wave resonances. Mostly, the resonances were modulated and some disappeared completely from the spectrum. It was not possible to investigate individual peaks for variations in the quality factors of the peaks because of the strong effect the defects had on the resonances.

7

The defects influence the spectrums of the silicon nitride balls mainly in the following ways:

- Scrambling of resonances

- Disappearance of some resonances

- Noisy signals associated with resonances

- Decrease of the signal at resonance

- Appearance of new resonances

Some examples of results obtained using this technique are shown in Figures 4 through 14, on the following pages. The balls are 7/16 in. NBD-200, from CERBEC (now Norton Advanced Ceramics) Lot # 922563.03.

Ball H
Perfect Ball
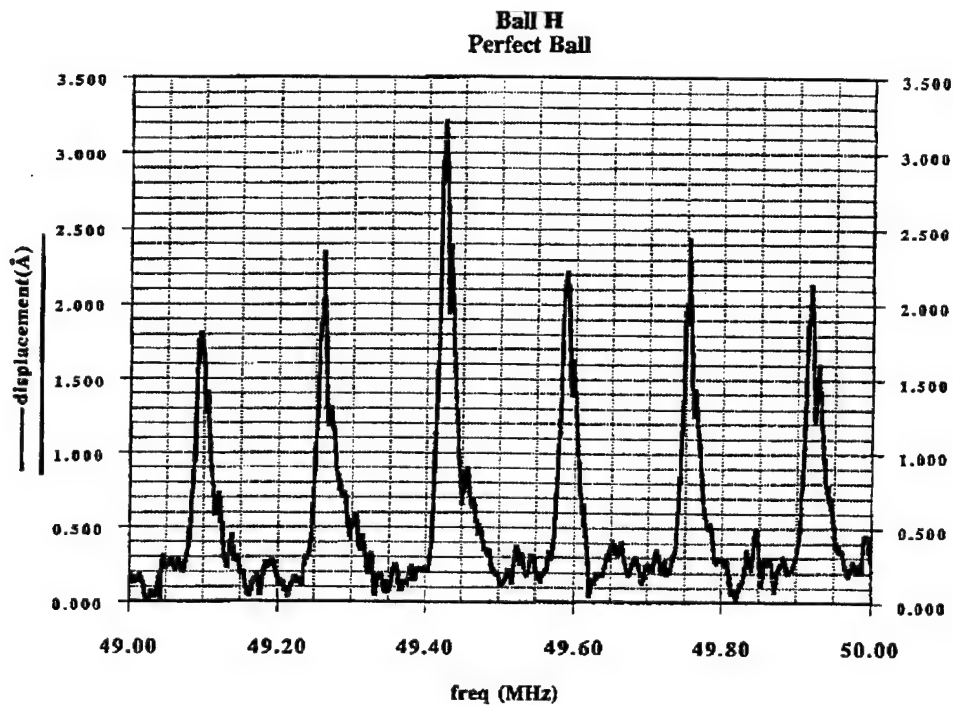
Figure 4: Resonant Spectrum, 7/16 in. NBD-200 Ball
Lot# 922563.03, No Defects

8
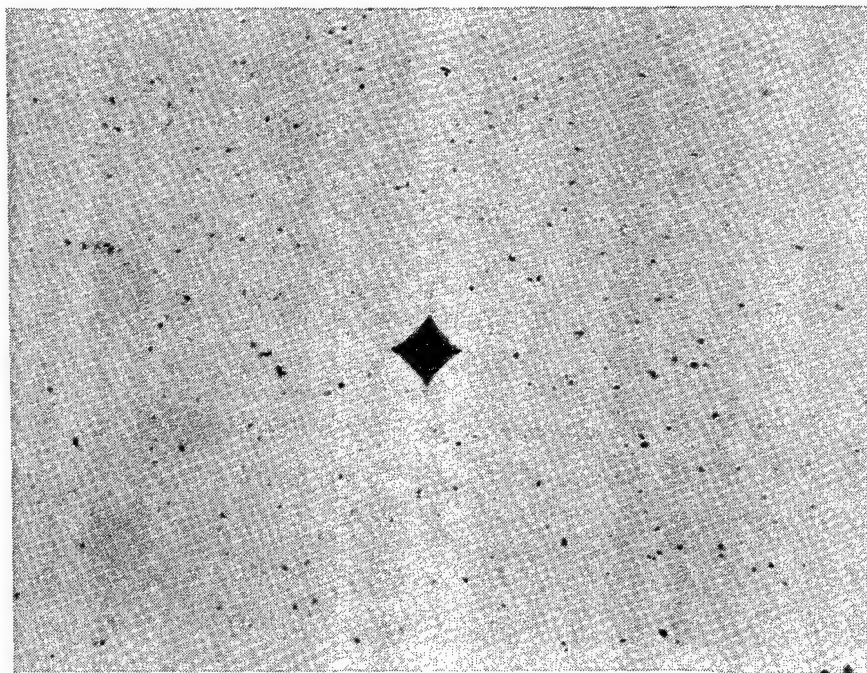
Figure 5: 7/16 in. NBD-200 Ball, Lot# 922563.03
One 0.5 Kg Vickers Indent, 450x Magnification
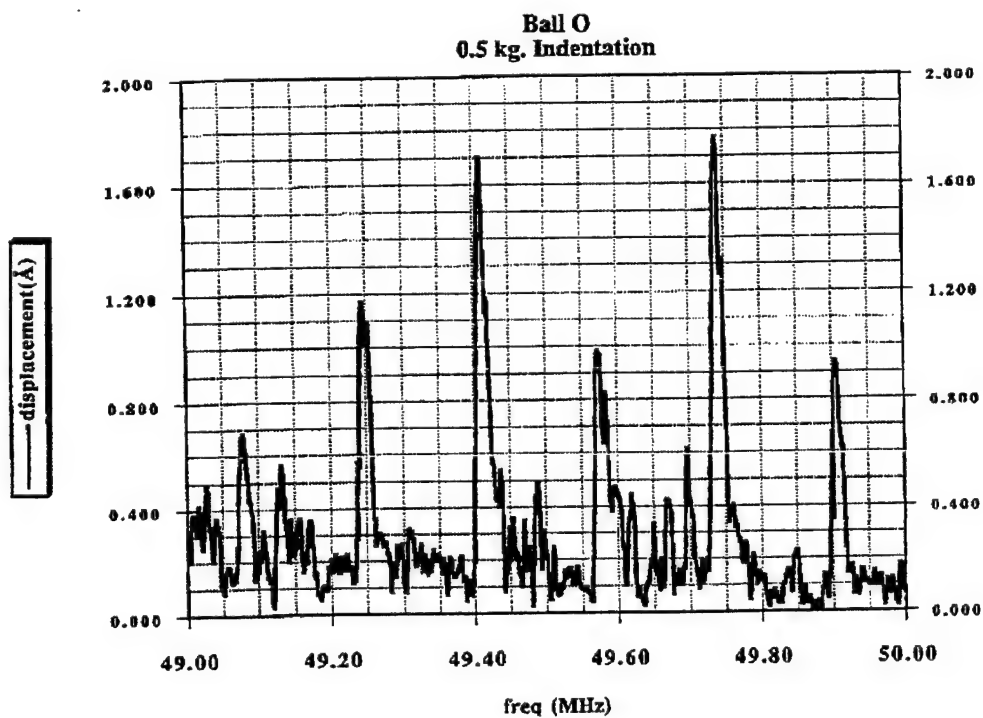
Figure 6: Resonant Spectrum, 7/16 in. NBD-200 Ball
Lot 922563.03, One 0.5 Kg Vickers Indent
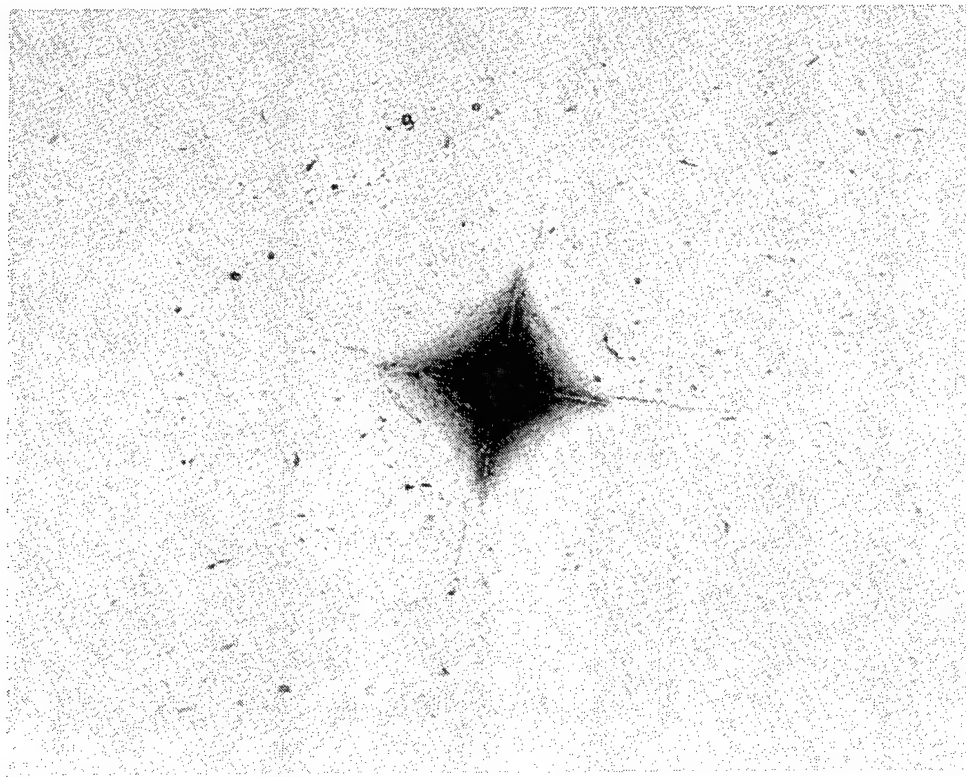
Figure 7: 7/16 in. NBD-200 Ball, Lot# 922563.03
One 5.0 Kg Vickers Indent, 450x Magnification
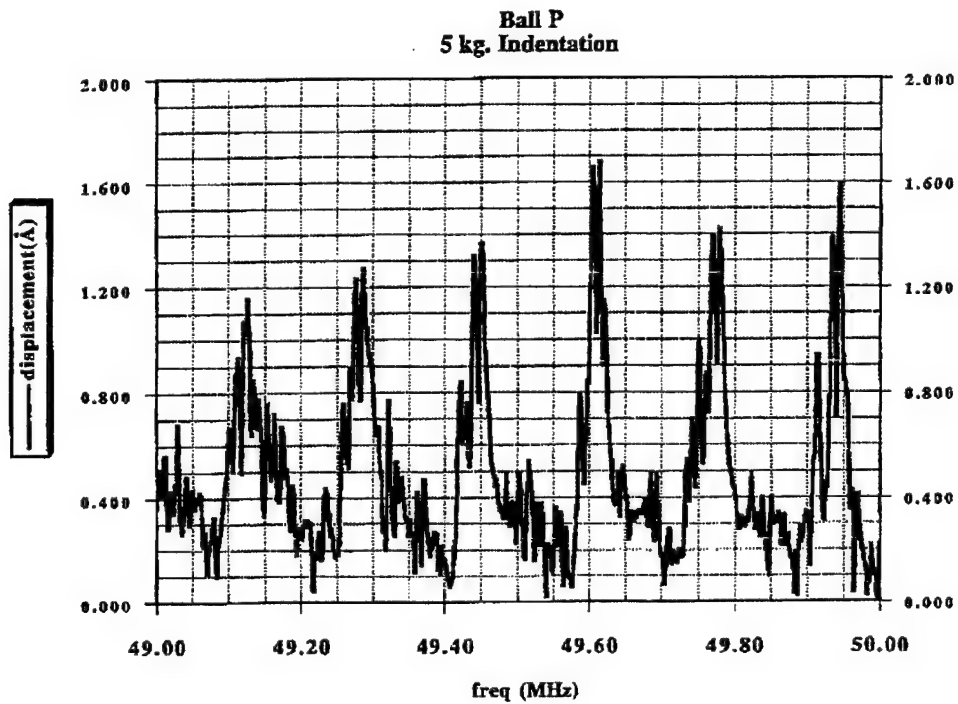
Figure 8: Resonant Spectrum, 7/16 in. NBD-200 Ball
Lot 922563.03, One 5.0 Kg Vickers Indent
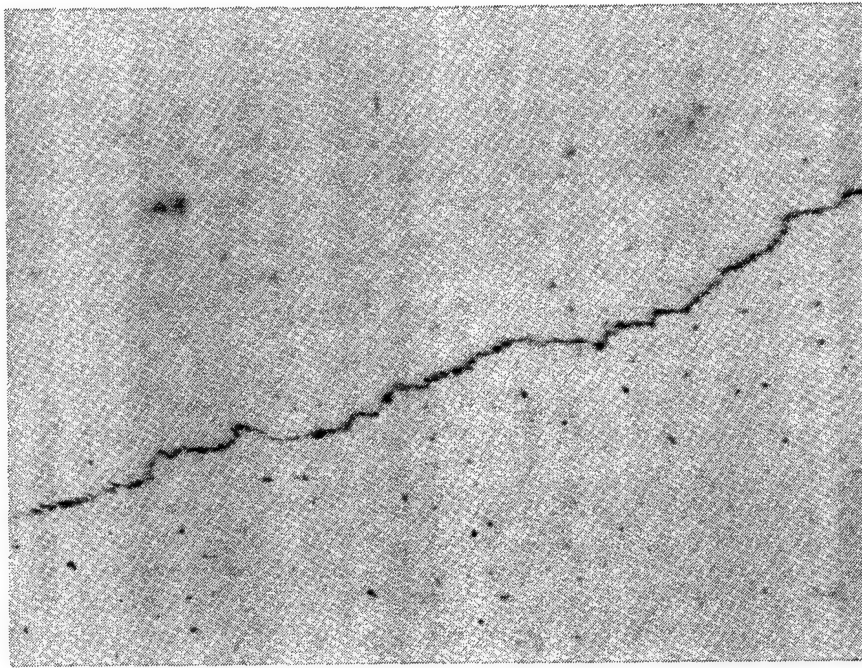
Figure 9: 7/16 in. NBD-200 Ball, Lot# 922563.03
Meandering Scratch, 450x Magnification
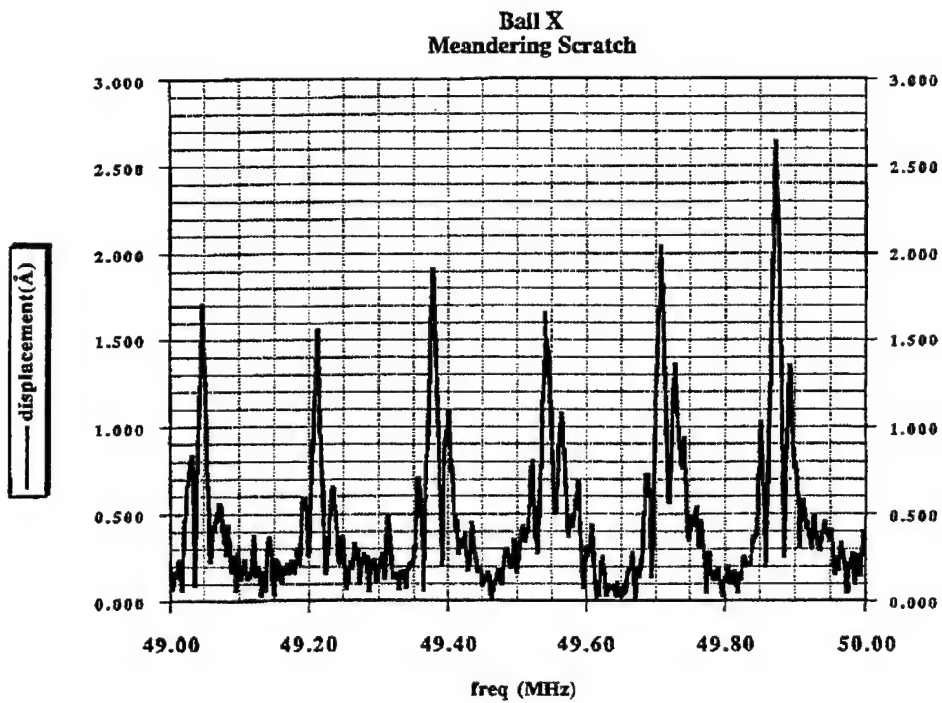
Figure 10: Resonant Spectrum, 7/16 in. NBD-200 Ball
Lot# 922563.03, Meandering Scratch

11
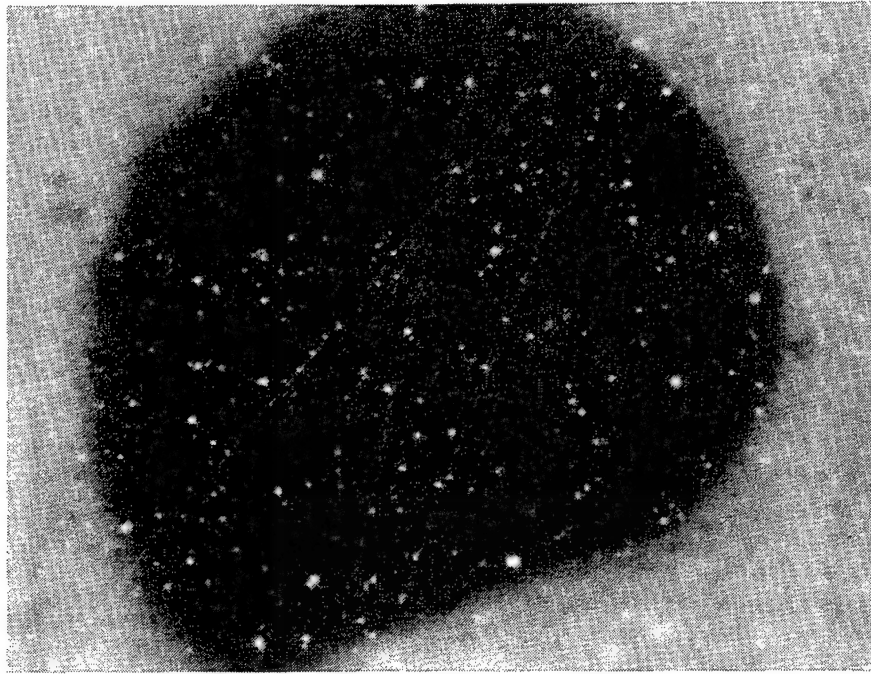
Figure 11: 7/16 in. NBD-200 Ball, Lot# 922563.03
Iron Rich Area, 450x Magnification
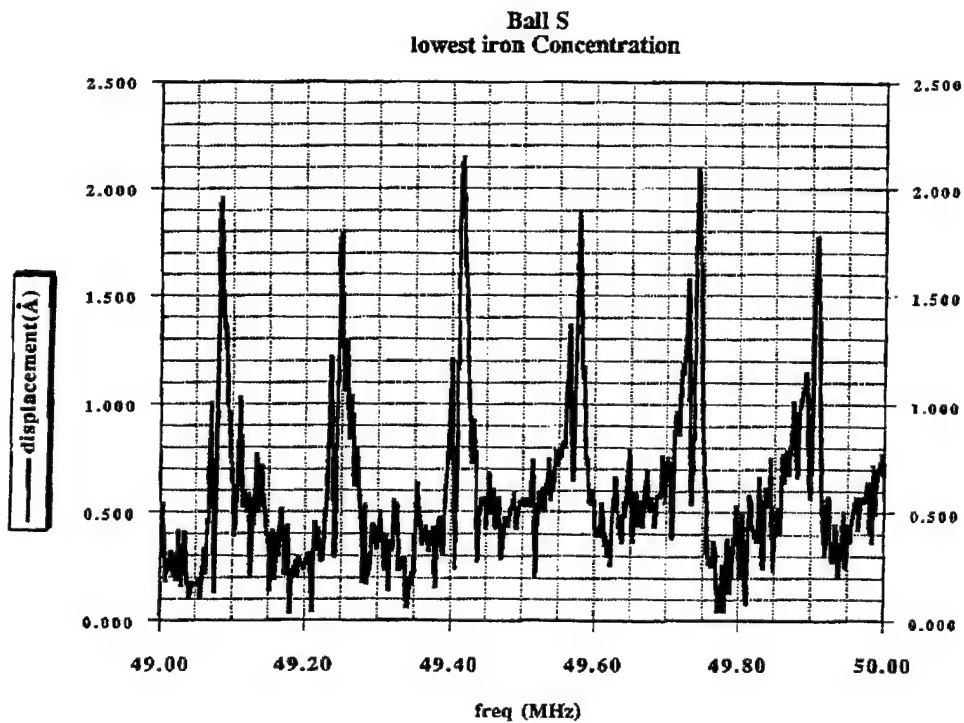
Figure 12: Resonant Spectrum, 7/16 in. NBD-200 Ball
Lot 922563.03, Iron Rich Area
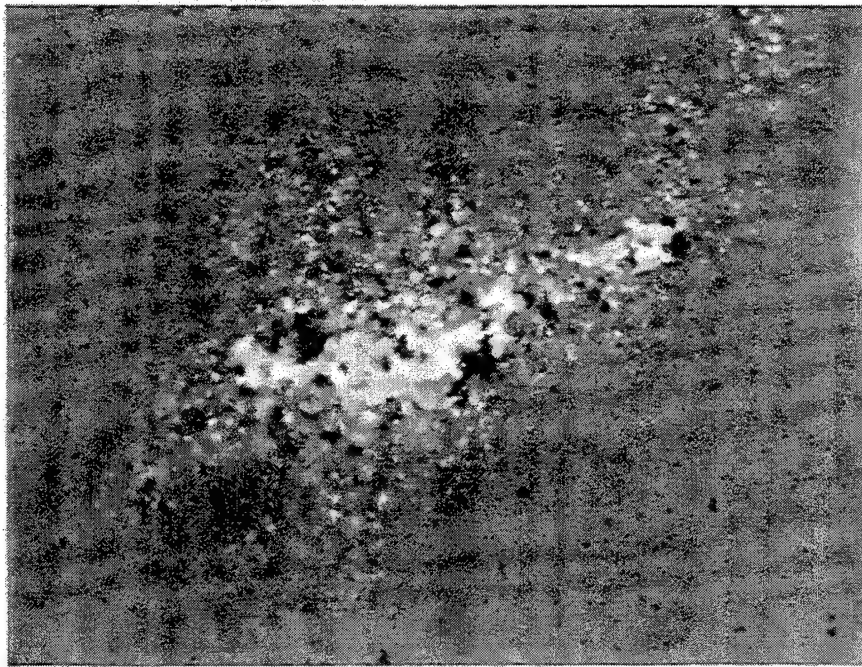
Figure 13: 7/16 in. NBD-200 Ball, Lot 922563.03
Large Iron Inclusion, 450x Magnification

Ball U
Large Iron Concentration
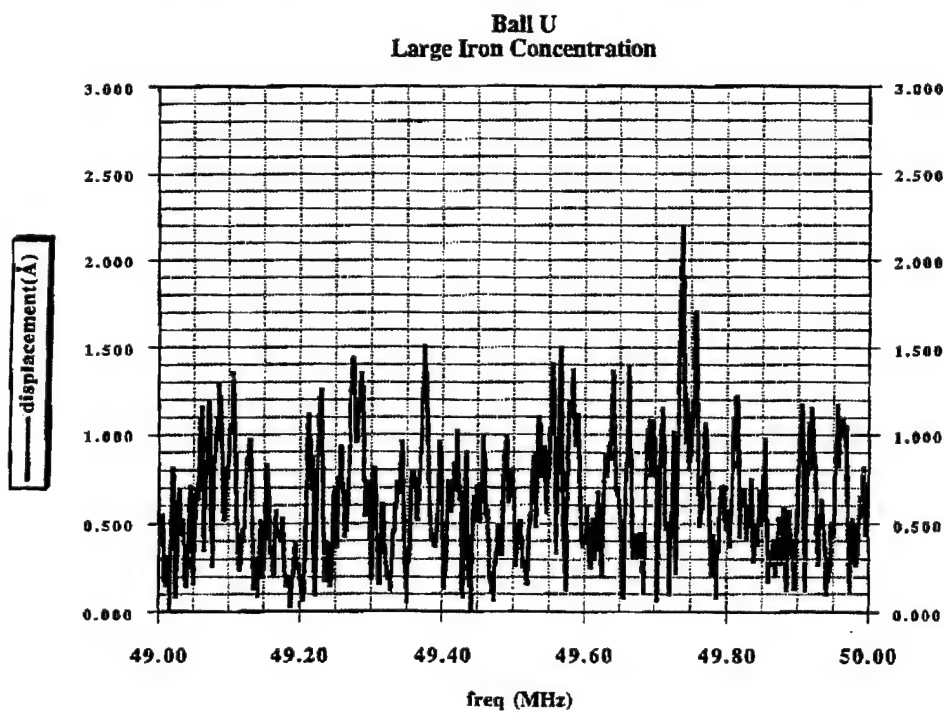
Figure 14: Resonant Spectrum, 7/16 in. NBD-200 Ball
Lot 922563.03, Large Iron Inclusion

13

Figure 4 shows the resonant spectrum for a ball with no defects found in the optical inspections normally used. Note the resonant frequencies and that the maximum amplitude of any resonance is 3.2 Å.

Figures 5 through 8 show results for single Vickers Indents using 0.50 and 5.0 Kg loads. For these defects, the following can readily be seen:

- A reduction in maximum amplitudes

- An increase in noise levels between the resonances

- Disappearance of some of the resonances

- Shifting of some resonant frequencies

Figures 9 and 10 show results for a "meandering scratch" on the ball. This type of scratch is very superficial and is associated with certain ball cleaning processes. This type of scratch is not performance limiting in silicon nitride balls. As before, an increase in noise levels, reduction in amplitudes, and some shift in resonances occurs.

Figures 11 through 14 show results for two levels of iron inclusions. These occur very rarely and were found by standard optical inspections. The iron rich area shows increase in noise levels and reduction in amplitudes. The most interesting result is for the large iron inclusion. This is 80 μm (0.0032 in.) in size and definitely performance limiting. For this defect, we see the disappearance of all resonances and an increase in noise levels for all frequencies scanned.

4.0 NDE AND LIFE TEST OF BALLS: TASK 3.1.6s

Following these initial results, another production lot of 7/16 in. NBD-200 balls, Lot# 932766.02, was investigated. The object was to classify these balls by considering their spectra and by comparing these spectra to those of the balls with artificial defects.

A quantity of 250 balls was tested. Initially, measurements on the same ball were very difficult to reproduce, when a ball was removed and replaced over the acoustic transducer. This resulted in several major overhauls of the optics, acoustics and electronics because a system malfunction was suspected. Several of the previous balnls were also tested. The results obtained on those balls were reproducible with some minor variations. Repeatability problems were not due to the system, but rather to the fact that many of the balls had small compression crack defects on the surface due to some manufacturing steps. The characterization and source of these defects is dealt with in Volumes One and Three of this document. It is important to note that, as the position of a ball was changed with respect to the test set-up, different resonant spectra were measured. Several discussions were conducted with Charles Burk of Norton Advanced Ceramics. A decision was made to continue the tests with this manufacturing lot. Tests were continued and the balls were rated according to empirical criteria, outlined below.

All 250 balls were measured and rated. For "good" balls, the measured resonant frequencies agreed reasonably well with the theoretical predictions. For certain "bad" balls, the resonance of Rayleigh and/or whispering gallery waves were split into multiple peaks. Turning the ball under the same condition changed the shape of the multi-peak signal. This phenomenon could be ascribed to asphericity, i.e., geometric deviation from a perfect sphere, which modified the phase condition for resonance. "Bad" balls with surface and near-surface defects tended to scatter energy from the Rayleigh mode into other resonant modes. The degree of "badness" of a ball may be evaluated by the degree of "scrambling" of the signal and by the amount of deviation of the experimental measurements from theoretical predictions. The higher-order modes were more sensitive to defects than Rayleigh mode and it is these modes that "scrambled" first.

15

Other evaluation criteria were also examined and these included variation in resonance amplitudes, resonance Qs', changes in apparent surface wave velocity, spacing of resonances, and disappearance of resonances.

All these considerations led to establishing the following protocol to rate these balls: In a certain frequency range, the number, spacing and sharpness of the peaks whose amplitudes exceed half of that of the highest resonant peak are examined. Any major deviation of the character of those peaks from a clean signal can be ascribed to a defective ball. For instance, a splitting in any of these peaks is due to strong asphericity, whereas any disappearance or major deviation in spacing or coupling into other resonant modes of these peaks is ascribed to major surface or near-surface defects.

If a ball passes this initial "screening" test, it is examined further by looking at the peaks whose amplitudes exceed one third of that of the highest peak. The same evaluation criteria are followed. In this case, any deviation from a clean signal is ascribed to a lesser degree of "badness". Figures 15 to 19 show examples on how this protocol is applied to specific defect and asphericity cases.

The balls rated using this protocol were then sorted into eight complements of 28 balls each. Table 1 shows the sorting, which was some attempt to put the "best" balls into the complement for Test Bearing One, progressing to the "worst" balls in Test Bearing Eight. The 228 balls were selected in this way for testing. The 32 balls rated most poorly were not used in the life testing. Life testing was performed at Timken Research and results are reported in Volume One of this document.
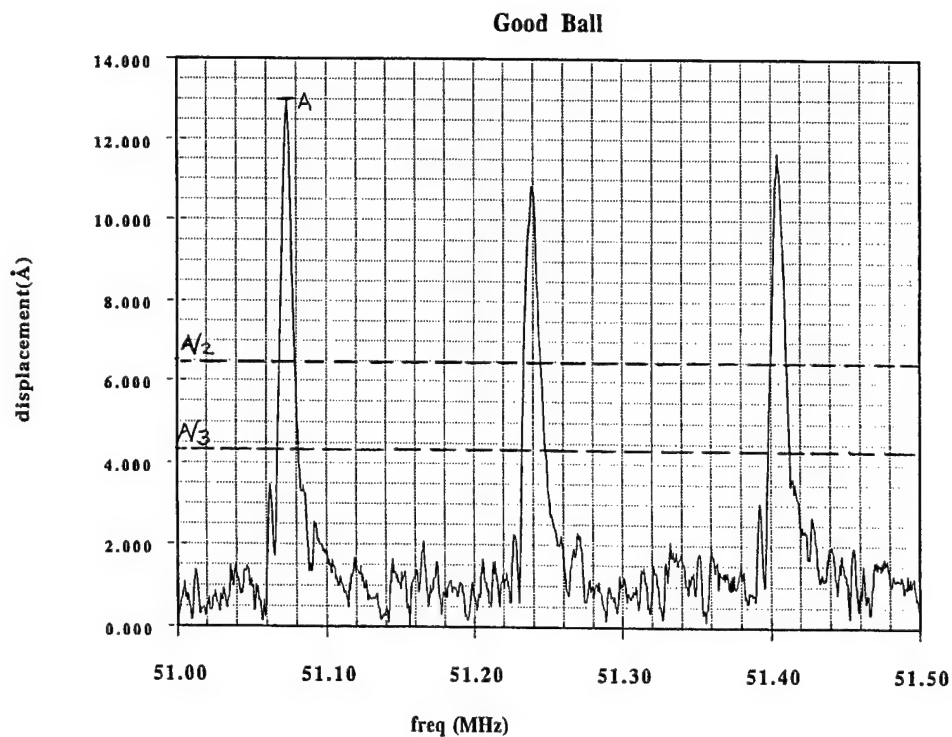
Good Ball

Figure 15: Resonant Spectrum , 7/16 in. NBD-200 Ball
Lot 932766.02, "Good" Ball

Ball with Slight Asphericity
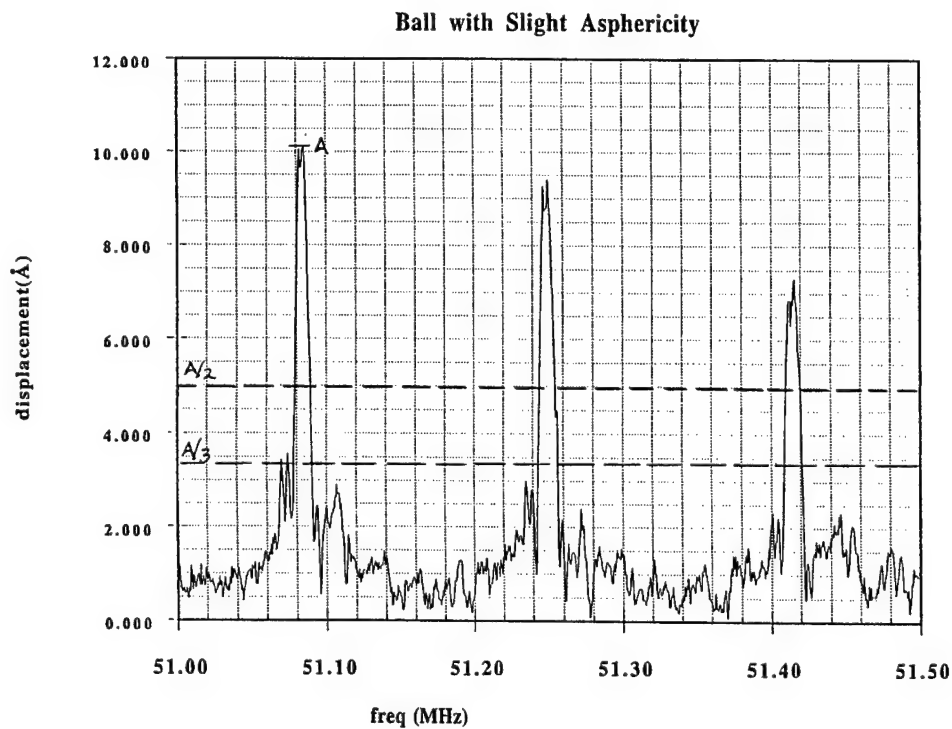
Figure 16: Resonant Spectrum, 7/16 in. NBD-200 Ball
Lot 932766.02, Slight Asphericity

17

Bad Ball: Slight Defects
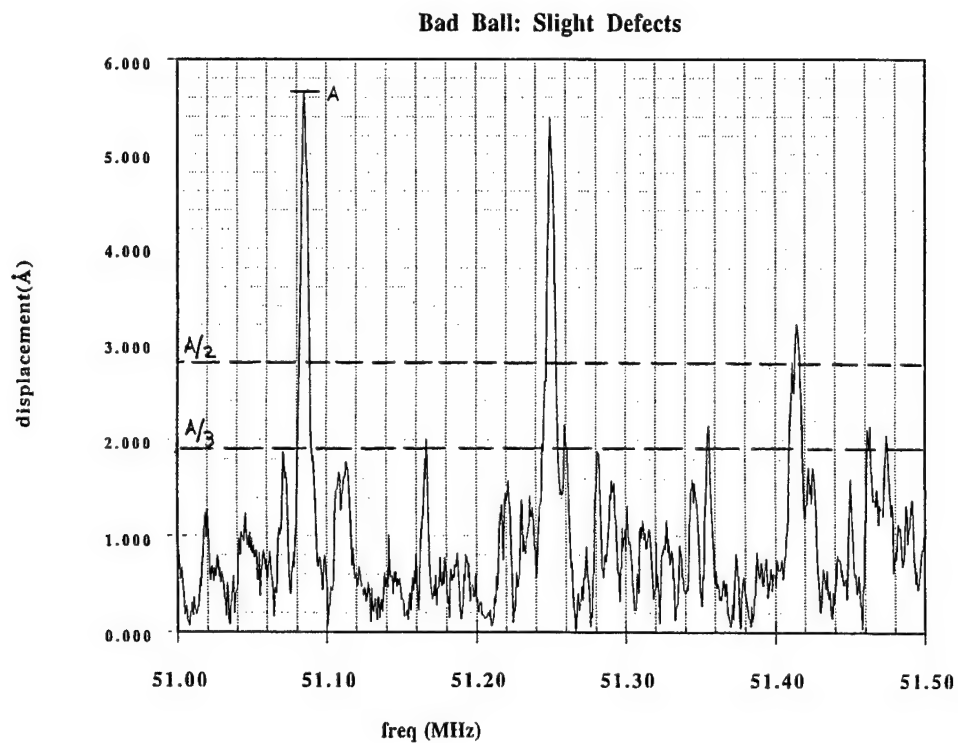
Figure 17: Resonant Spectrum, 7/16 in. NBD-200 Ball
Lot 932766.02, Slight Defects

Bad Ball: Severe Asphericity
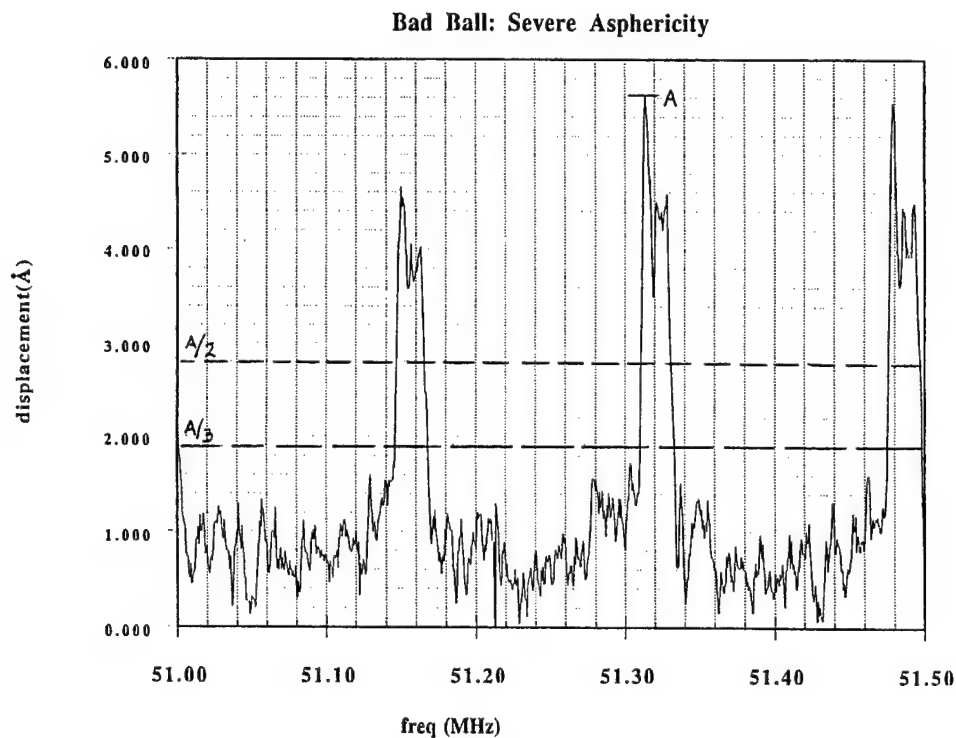
Figure 18: Resonant Spectrum, 7/16 in. NBD-200 Ball
Lot 932766.02, Severe Asphericity

18

Bad Ball: Severe Defects
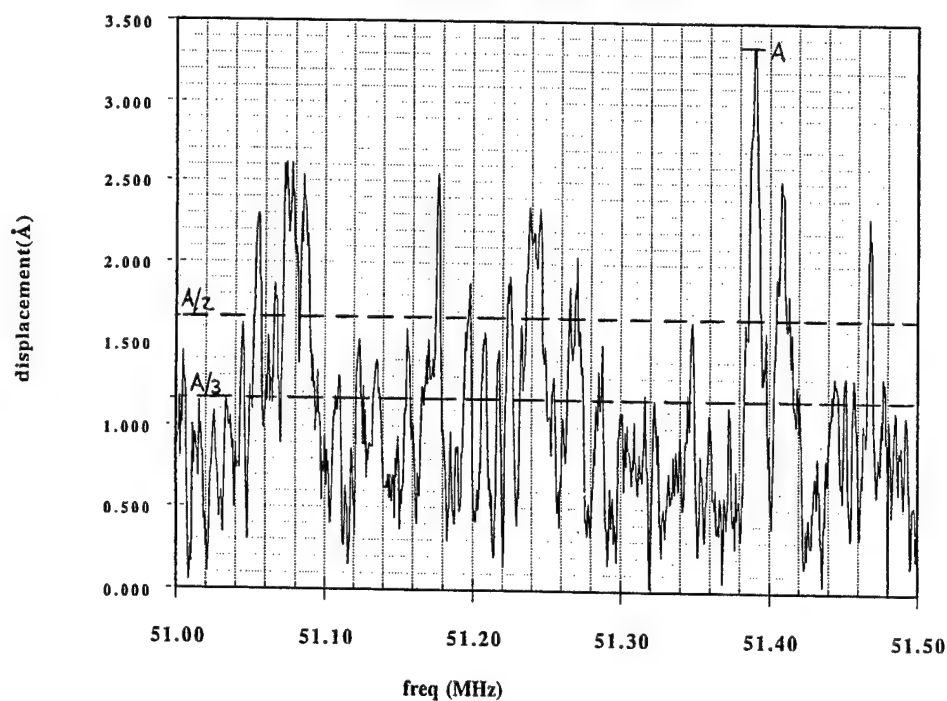
Figure 19: Resonant Spectrum, 7/16 in. NBD-200 Ball
Lot 932766.02, Severe Defect

Table 1: Surface Acoustic Wave Ratings 7/16 in. NBD-200
Balls, Lot 932766.02 28 Balls/Bearing Set

BRG & SET	DEFECT RATING				ASPHERICITY RATING			
	NONE	SLIGHT	MODERATE	SEVERE	NONE	SLIGHT	MODERATE	SEVERE
SET 1								
BRG 1	X				X	X	X	
BRG 2	X	X	X		X	X	X	
BRG 3			X			X	X	
BRG 4			X				X	
SET 2								
BRG 5			X				X	
BRG 6			X				X	X
BRG 7	X		X		X		X	
BRG 8				X			X	

19

5.0 PROGRAM RESULTS AND CONCLUSIONS

1. A system for measuring the resonant spectra of spheres in the frequency range of dc-80 MHz was developed. The system utilized a single point contact and thus minimized the influence of coupling sound into the balls.

2. At low frequency, shear and torsional resonance can be used to determine the material properties of a ball. However, operating in this region is insensitive to surface defects.

3. Over 300 balls were inspected at higher frequency and a protocol was developed for distinguishing good balls from balls with asphericity and balls with surface defects. Results show that asphericity results in splitting of the surface wave resonant peaks, and surface defects result in the introduction of new resonant peaks between those of the surface waves.

4. The system was quite sensitive, maybe too sensitive. Variations in the spectra often resulted when a ball was retested. This may be due to slight asphericity as different points on the sphere are used as "south pole" and "north pole". Unfortunately, no "perfect balls" could be obtained to test the system and to develop a more precise protocol. The detection system was tested on other types of ultrasonic devices and was found to work as predicted down to displacements of the order of 0.001Å.

5. A theoretical formalism was developed to determine the frequency of the surface wave resonant modes and those of the first several orders of "whispering gallery" modes. These are of interest because their energy is concentrated within a wavelength or so from the surface of the ball. There is very good agreement between the theoretical predictions and measurements of these resonant frequencies.

6. The system as developed is not limited to spherical objects or to ceramic objects. Further work should be done to determine the true value of this technology. It is superior to existing technologies because of the single contact, wide frequency range of operation, and ability to handle balls or other objects of any size. The merit of this system was not fully developed due to a number of unusual circumstances.

20

7. Although the system was not completely effective in detecting all defects that were life limiting, the work accomplished under this contract has led to numerous improvements in manufacturing procedures for NBD-200 silicon nitride balls. This is a very important program benefit.

8. It is strongly recommended that further work utilizing this technology be conducted on-site at a manufacturing facility that produces silicon nitride balls. In this way, iterative improvements in both this inspection method and the product inspected will be achieved most rapidly.

Appendix

Laser-Ultrasound:
One-Point-Contact Measurement

A.1.0   INTRODUCTION

In the previous work, we described the method of the contact-contact resonance sphere technique. This technique is operable in two frequency regions. In the low frequency region, the technique can accurately characterize (one in 104) acoustic material properties such as longitudinal wave velocity, shear wave velocity, and Poisson's ratio. In the high frequency region, where surface wave resonance dominates, it can be used to perform surface defect inspection. The existence of surface defects significantly reduces the quality factor of surface wave resonance modes. However, this technique has certain limitations, particularly in the measurement of small spheres. The first limitation is in the proper alignment of the two transducers, because the transducers are mounted on springs to simulate the free oscillation condition of the sphere. The second limitation is in controlling the contacting load between the transducers and the sphere. As the sphere gets smaller, the contact pressure and area between the transducers and the sphere can no longer be ignored. These problems can be circumvented by a one-point-contact measurement technique, in which the sample is supported by a concave depression in a buffer rod bonded to a transducer. This technique uses only one point to support the sphere as well as excite resonances on the sphere. The resonance signal is detected using an optical interferometer which measures the displacement of the top surface of the sphere, a non-contacting detection scheme.

A.2.0 EXPERIMENTAL SETUP

Figure A-1 shows the schematic of the one-point-contact technique. The ball is placed on a spherical depression (lens) in a buffer rod with a longitudinal piezoelectric transducer on the other end. The radius of curvature of the lens is larger than that of the ball, so that the ball can rest at the bottom of the lens. The transducer excites resonances on the ball and the interferometer measures vertical displacements of the waves on the ball at the opposite pole.
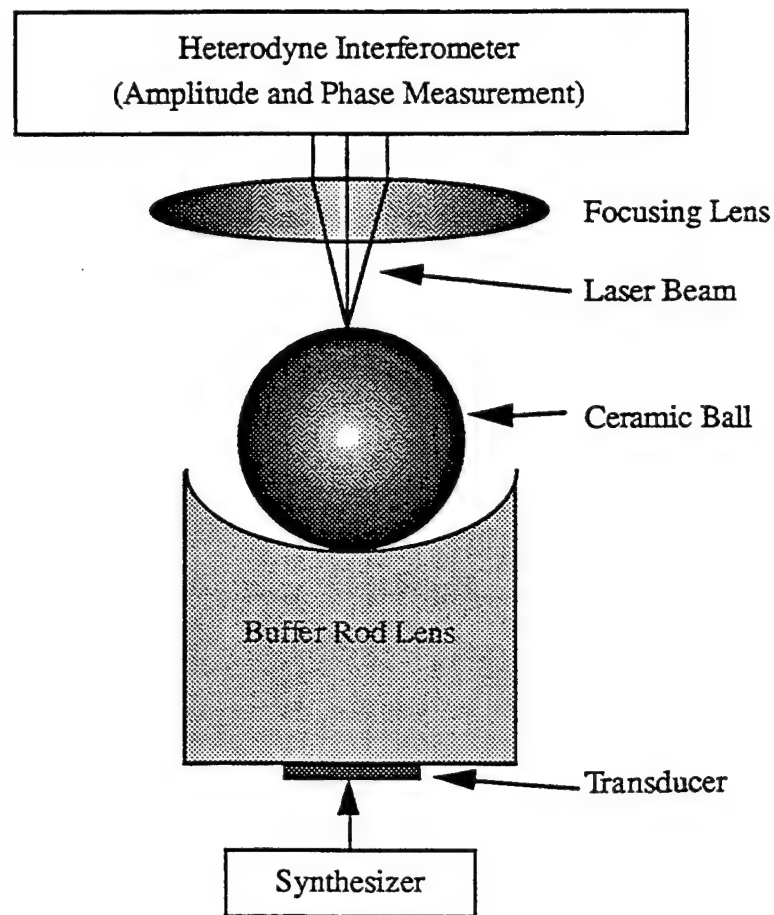
Figure A-1 One-Point-Contact measurement experimental setup.

23

A.2.1 Hertzian Contact

The only contact between the sphere and the external environment is a single Hertzian contact with a diameter of d given by[1]:

$$d = 2F^{\frac{1}{3}}\left(\frac{DRR'}{R-R'}\right)^{\frac{1}{3}} \qquad (1)$$

where

$$D = \frac{3}{4}\left(\frac{1-v^2}{E} + \frac{1-v'^2}{E'}\right) \qquad (2)$$

and R, v, E are the radius, Poisson's ratio, and Young's modulus of the lens, R', v', E' are the radius, Poisson's ratio, and Young's modulus of the sphere, and F is the total contact force (i.e., weight of the sphere).

For a fused quartz buffer rod, $v \approx 0.1694$ and $E \approx 7.274*10^{10} Newton/m^2$. For a hot isostatically pressed Si_3N_4 ceramic (NBD 200), $v'=0.2616$, $E'=3.223*10^{11} Newton/m^2$, and density$=3270 Kg/m^3$. In Figure A-2 we show two calculation results. The first one shows curves for contact diameter versus radius of a Si_3N_4 ceramic ball sitting on a fused quartz buffer rod. Each curve stands for a different radius of curvature of the depression on the buffer rod. In Figure A-2, we also show an extreme case where there is no depression (R = infinity). The second plot shows the contact diameter versus the radius of curvature of the concave depression on the buffer rod. We see that for each size of ball, the contact diameter varies only slowly with the radius of curvature of the depression when it is sufficiently larger than the radius of the ball.

For example, with $R=4$mm, a 1mm diameter ceramic ball with $R'=0.5$mm, we calculate $d=0.45\mu$m. At 60 MHz, where the surface wavelength on ceramics is around 100μm, the contact diameter is only about one percent of the wavelength, and thus has little effect on the propagation of surface waves.

To calculate the relationship between radius of ball and radius of curvature of the depression for most efficient surface wave excitation, the contact diameter should be equal to $\lambda_R/2 = V_R/(2 \cdot f)$, where f(Hz) is the operating frequency, and λ_R and
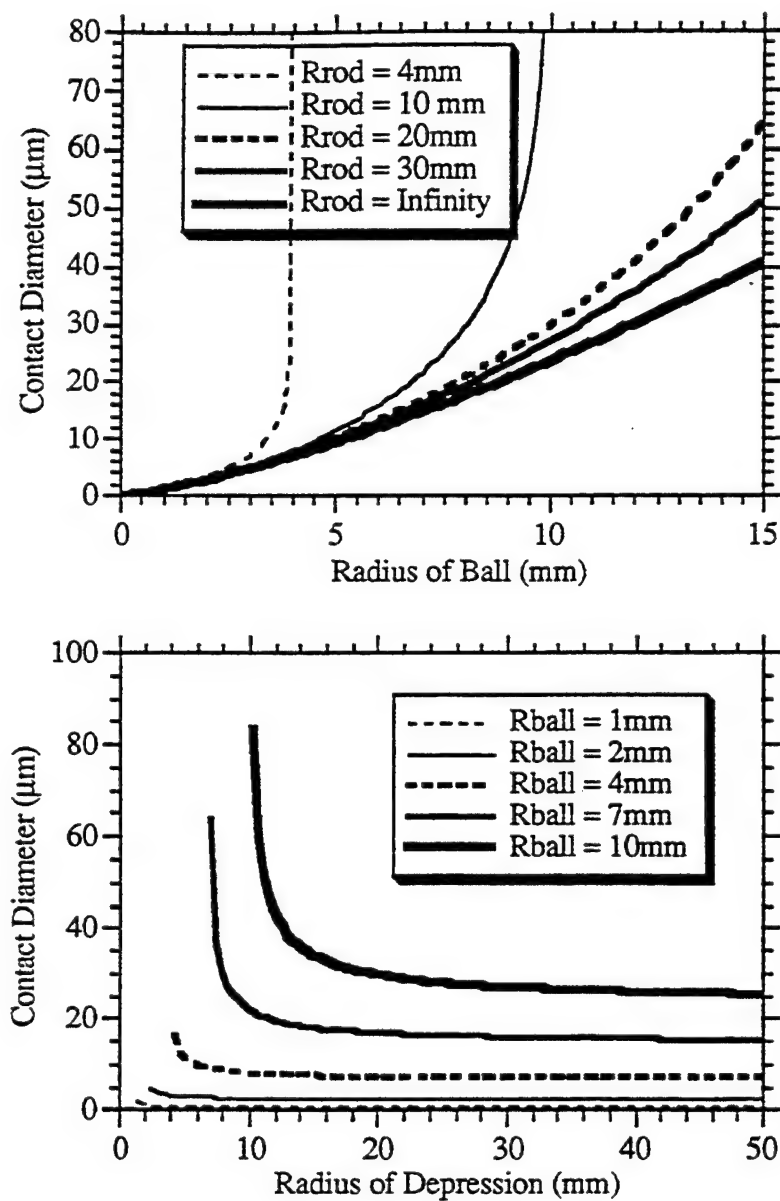
Figure A-2   (a) Hertzian contact diameter versus radius of
              ceramic ball.
            (b) Hertzian contact diameter versus radius of rod
              depression

25

V_R are the surface wavelength and surface wave velocity on the ball, respectively. For Si_3N_4 ceramics, V_R=5758.5-m/sec, the relationship between radius of ball R' and radius of curvature of the depression R for most efficient surface wave excitation is

$$R = \frac{R'}{1 - 5.5928 \cdot 10^{-17} \times f^3 \times R'^4} \tag{3}$$

Figure A-3 shows the optimum radius of curvature of the depression versus operating frequency for 5 particular radii of ceramic balls.
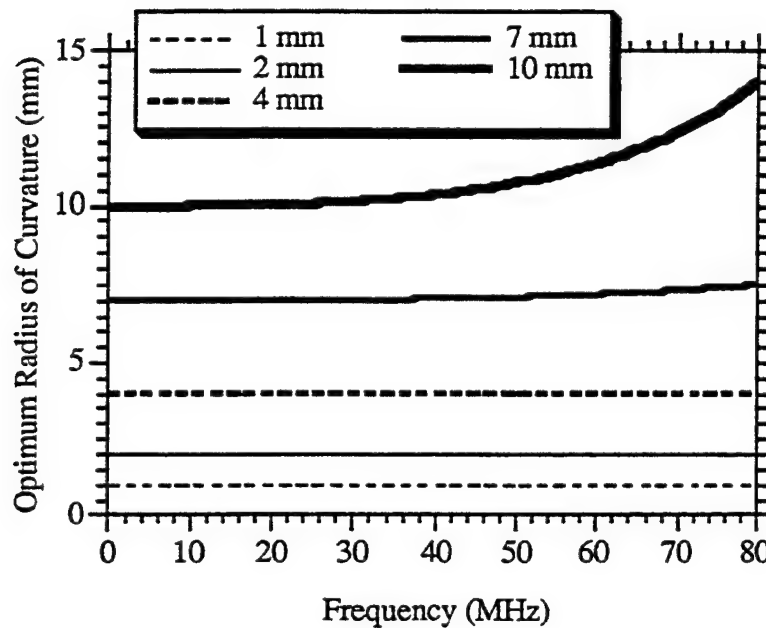
Figure A-3 Optimum radius of curvature of the depression versus operating frequency for 5 different radii of ceramic balls.

It is to be noted here that we are interested in measuring resonance spectra. Therefore, in order to keep the resonance Q high, the coupling to the ball should be weak. The contact diameter should be much smaller than 1/10 of the surface wavelength in order not to interfere with the propagation of surface waves. For fused quartz buffer rod and Si_3N_4 ceramic ball, the minimum radius of curvature of the depression becomes:

$$R > \frac{R'}{1 - 6.991 \cdot 10^{-15} f^3 R'^4} \tag{3.a}$$

Figure A-4 shows the minimum radius of curvature required for the depression on a fused quartz buffer rod with different radii of Si_3N_4 balls.
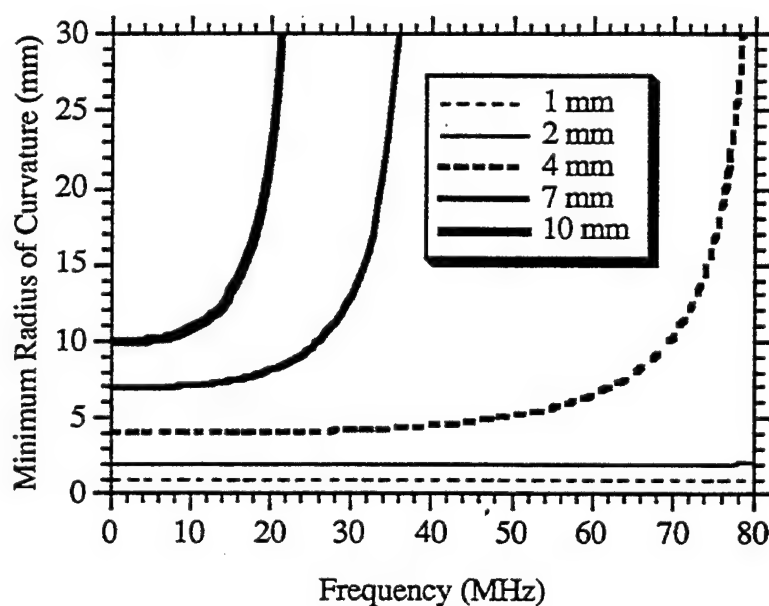
Figure A-4 Minimum radius of curvature of the spherical depression for a Hertzian contact less than 1/10 of surface wavelength.

We can also combine results of equation (3.a) with the condition for generating true surface waves that require $k_R a > 100$. For example, for a Si_3N_4 ball with a radius of 4mm, to generate true surface waves, the frequency has to be higher than 23MHz; this corresponds to a minimum radius of curvature required for the depression of only 4.089mm.

A.2.2 Advantages Of The One-Point-Contact Technique

The one-point-contact technique has advantages over the contact-contact technique because it does not require alignment of the two transducers. Also, the contacting load between the ball and the transducer is predictable. An experiment similar to the one-point-contact technique has been performed by Royer and Shui where a sphere was placed on a three-point mount and resonance was excited photoacoustically by a modulated laser beam[2]. The ball had a diameter of 20mm and was made of stainless steel with 13% chromium. They determined the shear wave velocity and the longitudinal wave velocity with a delay line method with an accuracy of 0.1% and measured V_s=3290m/sec and V_l=5988m/sec. They calculated V_R to be 3061-m/sec. They reported the observation of low frequency surface wave resonance modes up to $k_R a \approx 40$ which corresponds to a maximum operating frequency of 1.95 MHz.

One-Point-Contact has several advantages over the contact-contact method. First, the only connection between the sphere and the external environment is a Hertzian contact. The effect of Hertzian contact on the resonance of the sphere is adjusted for minimum contact of the transducer while still allowing maximum free oscillation of the sphere. Second, it is more efficient to excite resonance by a direct mechanical contact. The surface displacement of the transducer piezoelectric material $LiNbO_3$, (crystal-type trigonal 3 m, propagation along Z axis), active area 1 mm², center frequency 150 MHz, fused quartz rod length 30 mm, with an input of 1 volt, is shown in Figure A-5. The top plot shows a frequency response between DC and 5 MHz; the bottom plot shows a frequency response up to 300 Mhz. The resonant spectrum in the low frequency is due to resonance of the buffer rod; it disappears in the high frequency region because of attenuation inside the buffer rod. We see that we can acoustically excite a strong displacement on the ball. Since the photoacoustic effect on ceramics is very weak, to generate

28

surface waves using laser excitation will have the risk of damaging the sample. The laser for the interferometer in our setup is a He-Ne laser with a power of 4 mW and should have negligible thermal effect on the sphere. Therefore, the measurement can be done at a higher signal-to-noise ratio, compared to the photoacoustic method which is very inefficient on ceramics. Furthermore, because the sphere is always located at the bottom of the concave depression, alignment of the measurement system for different spheres of identical diameters becomes trivial. Finally, there is no limit to the frequency range over which the measurement can be made. We have measured up to a $k_R a$ value of 240, in this case, a 1/4 inch diameter ceramic bearing ball with an excitation up to 70 MHz.

A.2.3 Optical Detection And Heterodyne Interferometer

An excellent paper written by Jean-Pierre Monchalin reviews various optical methods to detect ultrasound at the surface of opaque solids[4]. Optical detection techniques for ultrasound can be classified into non-interferometric techniques and interferometric techniques. The former are well developed and of limited application, while the latter are more general and are presently the object of active developments.
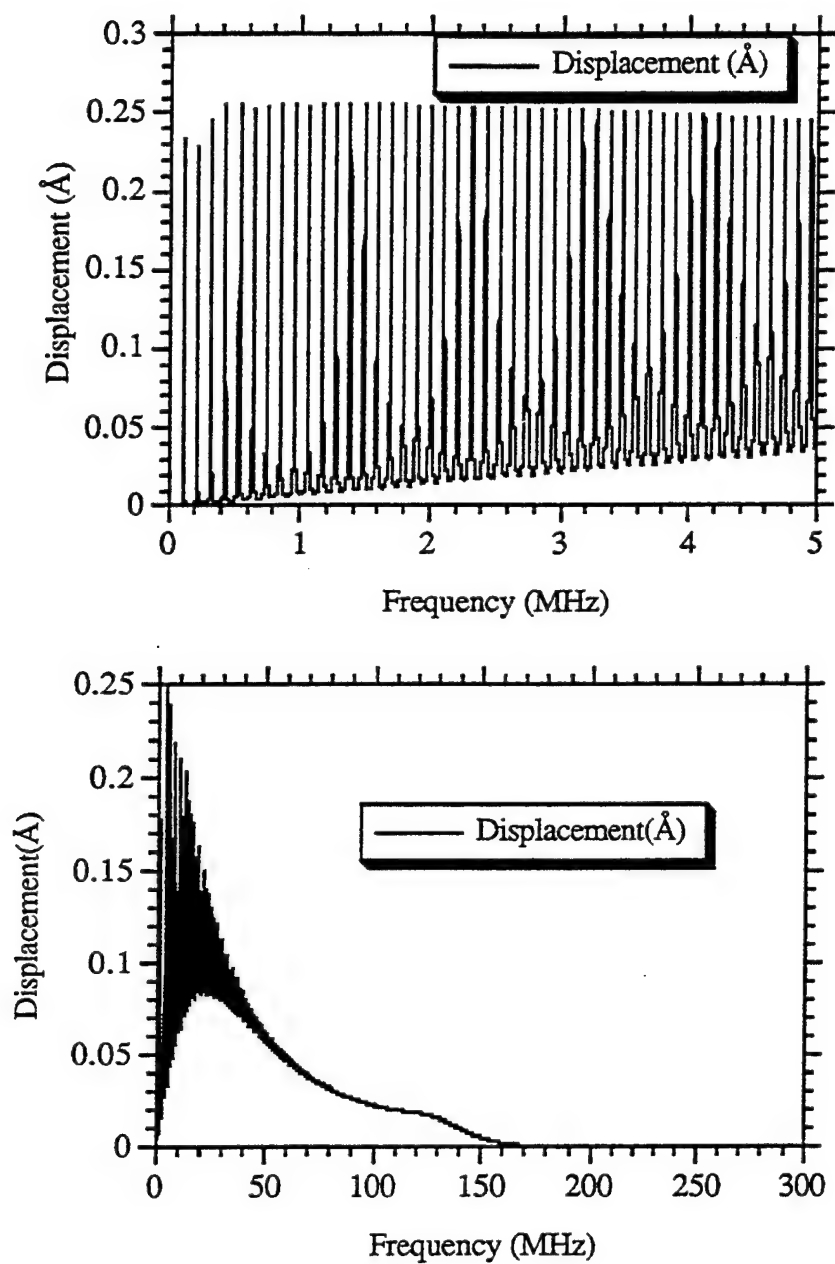
Figure A-5 Displacement of the transducer used. (LiNbO$_3$ crystal-type trigonal 3 m, propagation along Z-axis, active area 1 mm^2, center frequency 150 MHz, fused quartz rod length 30 mm, with an input of 1 volt).

There are several optical techniques used to detect
ultrasound that are not based on interferometry: the knife-edge
technique[5,6,7,8,9,10,11], the surface-grating technique[12,13], the
reflectivity technique[14,15], and a technique based on a light
filter[16,17]. All these techniques give a filtering bandwidth that
is fixed and determined by the medium, unlike interferometry,
which enables one to choose the most suitable bandwidth easily.

   There are various interferometric detection techniques that
can be classified into the following three types: optical
heterodyning interferometry[18,19,20,21,22], differential
interferometry[23,24], and velocity or time-delay interferometry[25,26].
Of these different interferometric detection techniques, optical
heterodyning interferometry is the most commonly used, and is
employed in our experiment. The configuration of our heterodyne
interferometer is shown in Figure A-6[27].
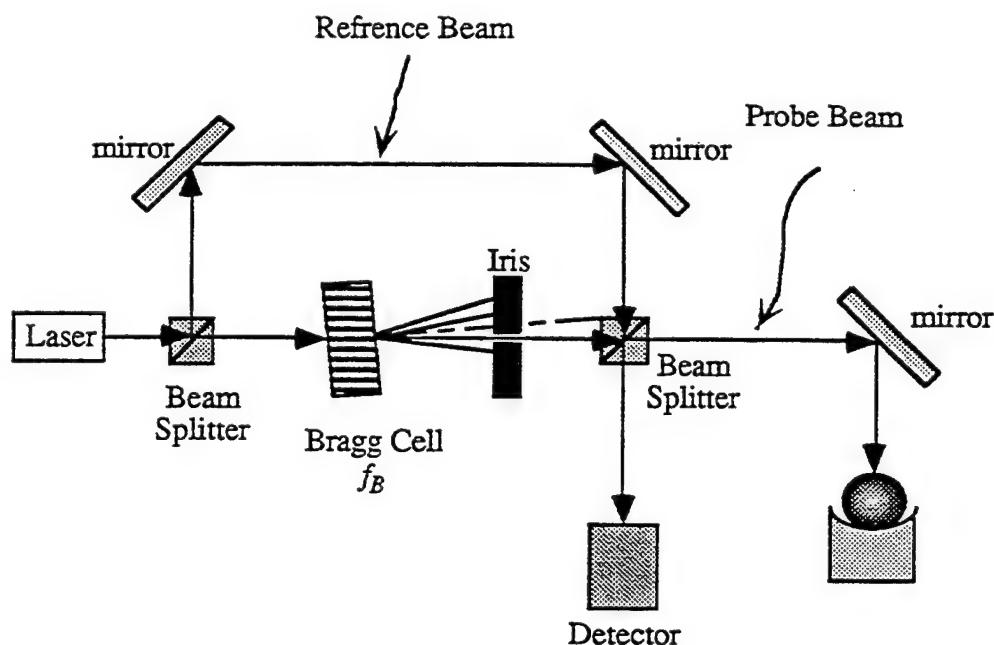
Figure A-6 Optical Heterodyne Interferometer configuration for
          spherical resonance detection.

31

The output of a low noise He-Ne laser is split into two parts. One part, the beam in the reference arm, is reflected twice by the two mirrors and sent directly into the photo detector. The second part is sent into a Bragg cell, an acousto-optic modulator, in our case driven at 80-MHz. The output from the Bragg cell consists of several diffraction beams[28]. An iris is used to pass only the first diffraction lobe which is frequency shifted by the Bragg cell frequency. The Bragg cell is rotated to an angle such that the first diffracted beam has maximum intensity, as shown in Figure A-6.

We call this first diffraction beam the probe beam. The probe beam is deflected by the mirror and reflected by the north pole of the resonating sphere. The optical phase of the reflected probe beam is modulated by the displacement $\mu cos(\omega_a t+\phi_a)$ of the resonating surface, where μ, ω_a and ϕ_a stand for maximum displacement amplitude, angular frequency, and phase of the acoustic displacement at the north pole of the sphere. Theoretically, it is possible to calibrate an optical heterodyne interferometer and measure both the amplitude and the phase of the displacement as will be shown in the following discussion.

We represent the reference beam sent to the photo detector by:

$$\hat{R} = R exp\left\{j\left[(\omega_L t+\phi_R+\phi_{RN})\right]\right\} \tag{4}$$

Where R, ϕ_R and ϕ_{Rn} are the amplitude, phase and phase noise of the reference beam, respectively, and ω_L is angular frequency of the laser. The reflected probe signal has the form:

$$\hat{S} = S exp\left\{j\left[(\omega_L+\omega_B)t+\phi_S+\phi_{SN}+2K_L u cos(\omega_a t+\phi_a)\right]\right\}, \tag{5}$$

Where ω_B is the angular frequency of the Bragg cell; S, ϕ_S and ϕ_{SN} are the amplitude, phase, and phase noise of the probe beam, respectively; and $K_L = 2\pi/\lambda_L$ is the wave number of the laser beam. For the He-Ne laser, $\lambda_L = 6325 Å$ and $K_L = 1/1007 (1/Å)$.

32

The photo detector detects the intensity of the incident light. Therefore, the output signal from the photo detector is:

$$
\begin{aligned}
\left|\hat{R}+\hat{S}\right|^2 &= \left(\hat{R}+\hat{S}\right)\left(\hat{R}^*+\hat{S}^*\right) = \\
&\left[R\exp\left\{j\left[(\omega_L t+\phi_R+\phi_{RN})\right]\right\}\right. \\
&\left.+S\exp\left\{j\left[(\omega_L+\omega_B)t+\phi_S+\phi_{SN}+2K_L u\cos(\omega_a t+\phi_a)\right]\right\}\right] \\
&\left[R\exp\left\{-j\left[(\omega_L t+\phi_R+\phi_{RN})\right]\right\}\right. \\
&\left.+S\exp\left\{-j\left[(\omega_L+\omega_B)t+\phi_S+\phi_{SN}+2K_L u\cos(\omega_a t+\phi_a)\right]\right\}\right]
\end{aligned}
\tag{6}
$$

where the asterisk stands for complex conjugate. Equation (6) can be simplified to be:

$$
\left|\hat{S}+\hat{R}\right|^2 =
\tag{7}
$$
$$
S^2+R^2+2SR\cos\left[\omega_B t+\phi_S-\phi_R+\phi_{SN}-\phi_{RN}+2K_L u\cos(\omega_a t+\phi_a)\right]
$$

For $K_L\mu\ll 1$ ($\mu \ll 1007\text{Å}$ for He-Ne laser),

$$
\cos\left[2K_L u\cos(\omega_a t+\phi_a)\right]\approx 1,
\tag{8}
$$

and

$$
\sin\left[2K_L u\cos(\omega_a t+\phi_a)\right]\approx 2K_L u\cos(\omega_a t+\phi_a)
\tag{9}
$$

Therefore, (7) can be expressed as follows:

$$
\begin{aligned}
&\left(S^2+R^2\right)+2SR\left\{\cos(\omega_B t+\phi_S-\phi_R+\phi_{SN}-\phi_{RN})\cos\left[2K_L u\cos(\omega_a t+\phi_a)\right]\right. \\
&\qquad\left.-\sin(\omega_B t+\phi_S-\phi_R+\phi_{SN}-\phi_{RN})\sin\left[2K_L u\cos(\omega_a t+\phi_a)\right]\right\} \\
&\approx\left(S^2+R^2\right)+2SR\left\{\cos(\omega_B t+\phi_S-\phi_R+\phi_{SN}-\phi_{RN})\cdot 1\right. \\
&\qquad\left.-\sin(\omega_B t+\phi_S-\phi_R+\phi_{SN}-\phi_{RN})\cdot 2K_L u\cos(\omega_a t+\phi_a)\right\} \\
&=\left(S^2+R^2\right)+2SR\left\{\cos(\omega_B t+\phi_S-\phi_R+\phi_{SN}-\phi_{RN})\right. \\
&\qquad-K_L u\left[\sin(\omega_B t+\phi_S-\phi_R+\phi_{SN}-\phi_{RN}+\omega_a t+\phi_a)\right. \\
&\qquad\qquad\left.\left.-\sin(\omega_B t+\phi_S-\phi_R+\phi_{SN}-\phi_{RN}-\omega_a t-\phi_a)\right]\right\}
\end{aligned}
$$

33

$$= \left(S^2 + R^2\right) + 2SR\cos\left(\omega_B t + \phi_S - \phi_R + \phi_{SN} - \phi_{RN}\right) \tag{10}$$

$$- 2SRK_L u\sin\left[\left(\omega_B + \omega_a\right)t + \phi_S - \phi_R + \phi_{SN} - \phi_{RN} + \phi_a\right]$$

$$- 2SRK_L u\sin\left[\left(\omega_B - \omega_a\right)t + \phi_S - \phi_R + \phi_{SN} - \phi_{RN} - \phi_a\right]$$

In expression (10), we see that the signal output from the photo detector consists of four parts: a dc signal, a signal with angular frequency ω_B, and two signals of equal amplitude but different angular frequencies, one at $(\omega_B + \omega_a)$, another at $(\omega_B - \omega_a)$.

Figure A-7 shows a typical picture of the output of a spectrum analyzer that monitors the output signal from the heterodyne
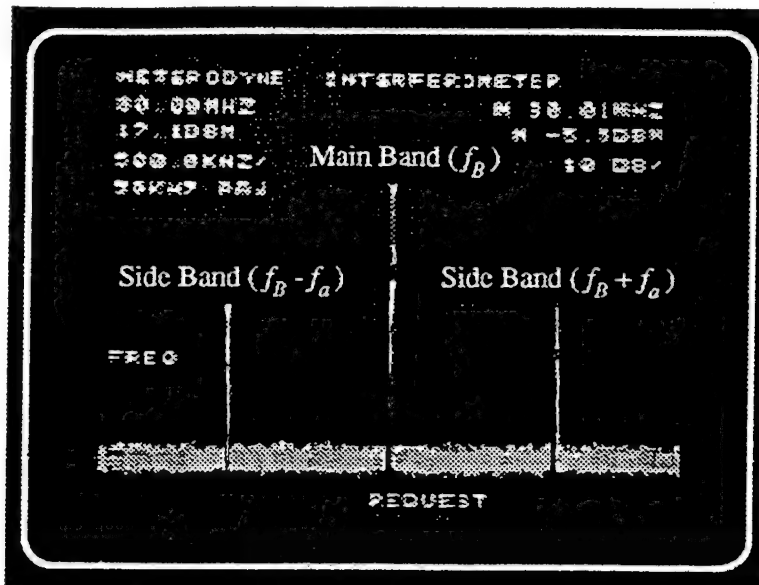
Figure A-7 A typical picture of the screen of a spectrum
           analyzer that monitors the output signal from a
           heterodyne interferometer.

interferometer as given by expression (10). In this case, the dc signal is blocked to protect the spectrum analyzer. As shown in the picture, the main band is the signal at 80 MHz, our Bragg cell operation frequency. The two side bands are of equal amplitude and with equal frequency distance away from the main

34

band. The frequency difference between the main band and the side band is the frequency of the acoustic signal on the sphere. From the last expression of (10), it is observed that the amplitude ratio between the main band and the side band is equal to $1/K_L\mu$. This means the heterodyne interferometer can be calibrated absolutely, and that

$$u = \frac{\text{Amplitude}_{\text{side band}}}{\text{Amplitude}_{\text{main band}}} \frac{1}{K_L} = \frac{\text{Amplitude}_{\text{side band}}}{\text{Amplitude}_{\text{main band}}} \frac{\Lambda_L}{2\pi} \tag{11}$$

where Λ_L is the wavelength of the laser. For He-Ne laser used in our experiment, $\Lambda_L = 632.8$nm. For this wavelength, equation (11) becomes:

$$u = 1007 \frac{\text{Amplitude}_{\text{side band}}}{\text{Amplitude}_{\text{main band}}} \text{ (Å)} \tag{12}$$

To perform broadband detection and acquire the amplitude and phase of the resonance signal, it is necessary to analog signal process the output signal from the interferometer. A schematic of the analog signal processing of the output from the heterodyne interferometer is shown in Figure A-8. The signal from the photo detector $(\omega_B, \omega_B \pm \omega_a)$ is dc bypassed and then split into two parts. The first part is sent into a phase locked loop. The output from the phased locked loop is an 80-MHz signal whose phase follows the variation of the main band. The second part is low pass filtered, so only $(\omega_B - \omega_a)$ is passed. These two signals are mixed. The result of the mixing operation is:

$$
\begin{aligned}
&2SR\cos(\omega_B t + \phi_S - \phi_R + \phi_{SN} - \phi_{RN}) \\
&\cdot 2SRK_L u \sin[(\omega_B - \omega_a)t + \phi_S - \phi_R + \phi_{SN} - \phi_{RN} - \phi_a] \\
&= 2S^2R^2K_L u \sin[(2\omega_B - \omega_a)t + 2(\phi_S - \phi_R + \phi_{SN} - \phi_{RN}) - \phi_a] \\
&\quad - 2S^2R^2K_L u \sin[\omega_a t + \phi_a]
\end{aligned}
\tag{13}
$$

The output from the mixer is seen to consist of two parts, one with an angular frequency of $(2\omega_B - \omega_a)$, another with an angular frequency of ω_a. This two part signal is low pass filtered so that only signal at the acoustic frequency is measured. It is observed that this signal is a scaled version of the acoustic signal, and is immune from the phase noise terms. The advantage of using the heterodyne interferometer becomes apparent at this

point, where it is apparent that this type of detection scheme is immune from environmental noise (fluctuations in phase). This acoustic signal is further processed using the method discussed in the contact-contact resonance sphere technique to determine both its amplitude and phase.
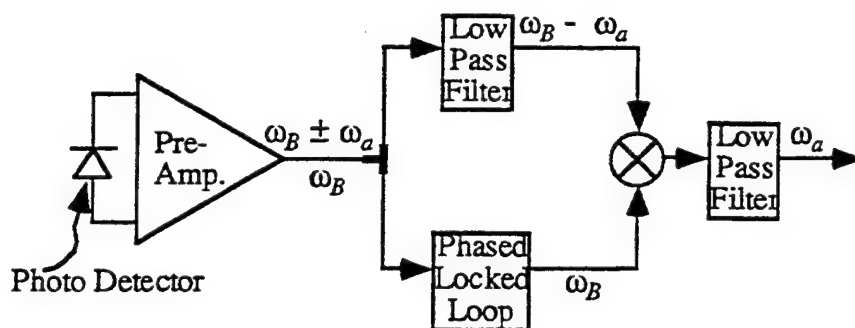
Figure A-8 Signal analysis of the output of the Heterodyne interferometer.

A.3.0   EXPERIMENTAL RESULTS

A.3.1   Low Frequency Measurement

To verify the results of the contact-contact resonance sphere technique and to qualify the one-point-contact measurement system, we first measured the low frequency spectrum of a 3/8 inch diameter Si_3N_4 ceramic bearing ball. The frequency spectrum in amplitude is shown in Figure A-9.
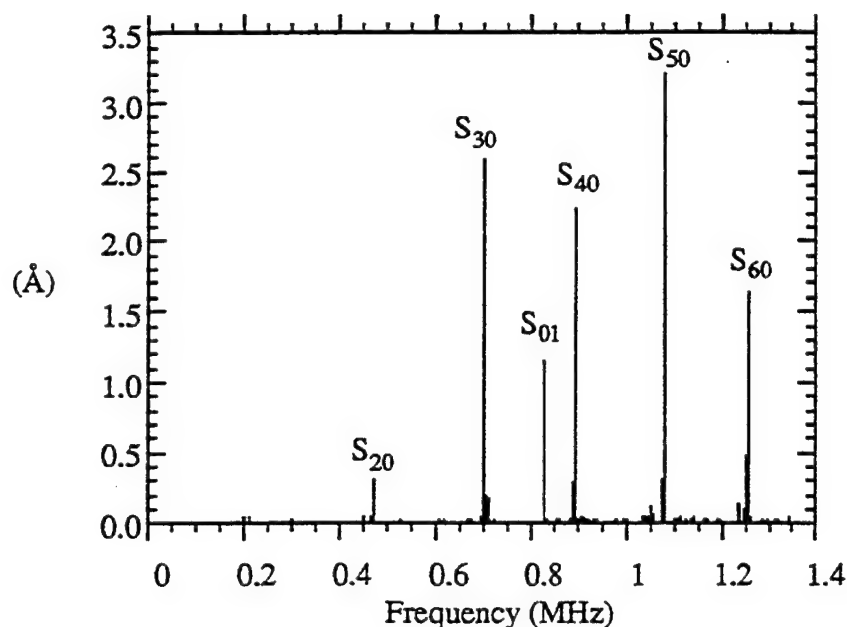
Figure A-9   Low frequency spectrum of a Si_3N_4 ceramic bearing ball with a diameter of 3/8 inch.

As seen in the figure, only the S_{n0} modes and the S_{01} modes are visible, while the torsional modes disappear. It is to be noted here that we are using a longitudinal wave transducer, the excitation is normal to the contact surface so no torsional mode should be excited. Even if we excite torsional modes using a shear wave transducer, since torsional wave resonances have no radial motion and their vertical displacement is equal to zero,

37

we will not be able to observe the torsional modes. This is
because the interferometer detects only the vertical displacement
of the surface. This also demonstrates one of the alignment
problems in the contact-contact measurement where we used
longitudinal transducers but still observed torsional wave
resonances. Comparing to the contact-contact measurement, the
one-point contact technique is incapable of observing the
torsional modes, but it has considerable advantages in the
control of alignment and loading, and yields reproducible
results.

A.3.2   High Frequency Measurement

. We have also used the technique to operate in the high
frequency region to observe surface wave resonances. We measured
three Si_3N_4 ceramic bearing balls with a diameter of 1/4 inch.
We first measured in the 30 to 35 MHz region where $k_Ra \approx 100$. The
results are shown in Figure A-10. As we can see in the figure
for the good ball, there is a series of equally spaced peaks.
The modulation of the peaks is probably due to the frequency
response of the transducer. Balls with cracks have a smaller
surface wave resonance amplitude. This is because the cracks are
scattering the surface waves. Part of the scattered energy goes
into bulk waves and does not contribute to the surface wave
resonance. The larger the surface defect, the more energy is
converted to bulk waves, causing the decrease of surface wave
resonance amplitude.

This interferometer can observe a frequency spectrum from around
10 KHz to about 70 MHz. The limit in the high frequency is due
to the physical operating frequency of the Bragg cell. To show
this capability, we measured the frequency spectrum of the same
three balls from 65 MHz to around 70 MHz. Figure A-11 shows the
result of this measurement.
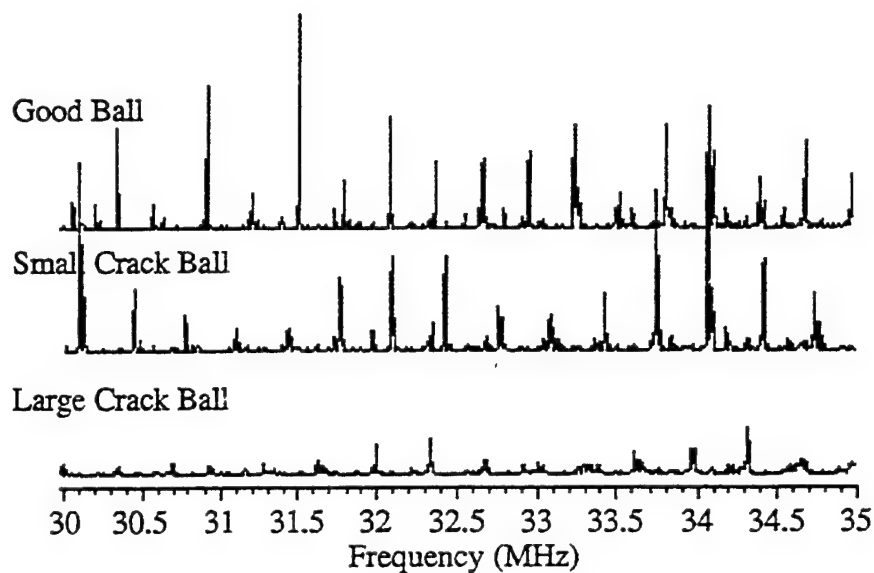
Figure A-10 Amplitude decrease due to existence of surface
            defects.
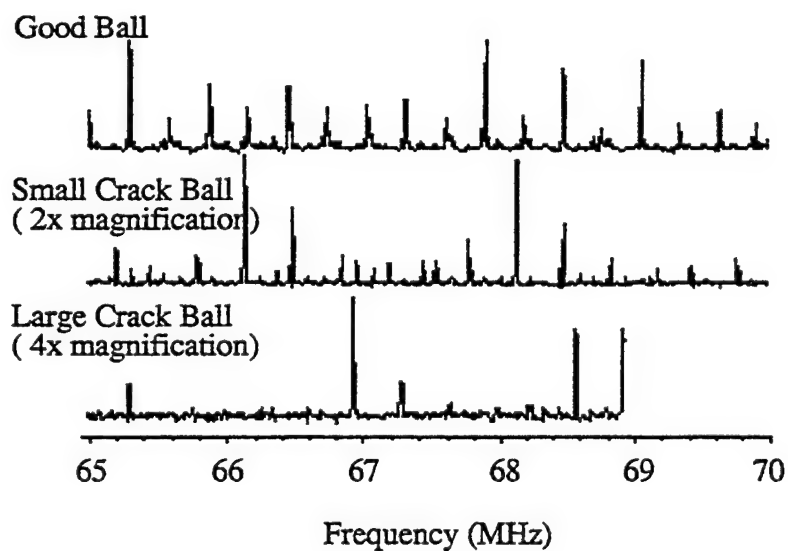
Figure A-11 Scrambling effect at high frequencies, we see some
            hybrid modes as well as the disappearance of some
            modes.

In Figure A-11, we again observe a series of equally spaced peaks for the good ball. For balls with defects, Figure A-11 shows a scrambling effect in the higher frequency range. New resonances appear at different frequencies. In this frequency range, surface cracks act like secondary sources of propagation of surface waves. Since waves passing by cracks suffer a phase change and an amplitude change, the primary wave generated by the transducer, and the secondary wave generated by surface cracks, interfere with each other, producing the scrambling effect observed. This phenomenon is illustrated in Figure A-12.
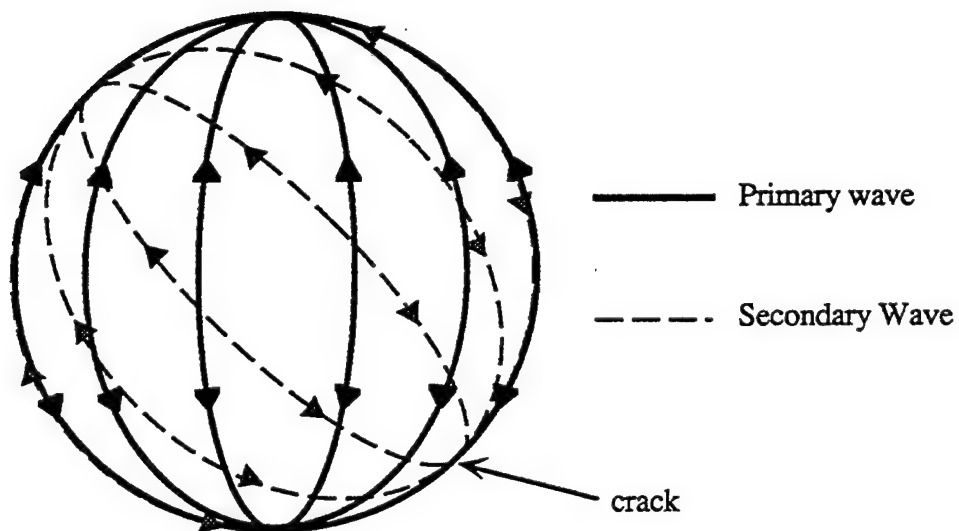
Figure A-12 Illustration of surface crack as a secondary surface wave source.

We also observed another phenomenon, an increase of apparent surface wave velocity with the existence of surface defects. The surface wave velocity V_R calculations show that the circumference of the sphere must be an integral multiple of surface wave length to form surface wave resonance:

$$\text{integer} = m = \frac{2\pi a}{\lambda_R} = \frac{2\pi af}{V_R} \qquad (14)$$

Therefore,

$$V_R = \frac{2\pi af}{m} \qquad (15)$$

where $m = n+2$ is the number of waves on the sphere.

The reason there is an increase in apparent surface wave velocity with the existence of surface defects is not yet clear. A hypothesis is that some surface waves get scattered back to the source before the waves have propagated one whole circumference. Therefore, the distance travelled becomes shorter, so the measured apparent surface wave velocity is larger. The result is shown in Figure A-13.

Figure A-13 Increase in apparent surface wave velocity with existence of surface defect. Curves of the small crack case and the large crack case are almost overlapped.

41

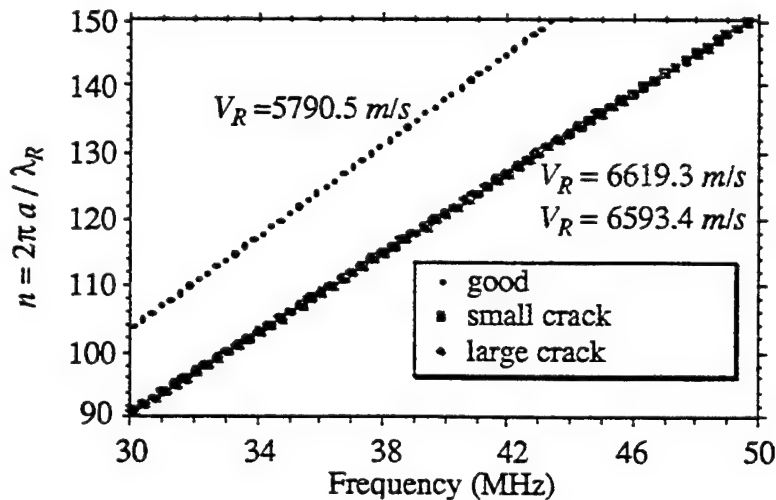Results from the above three figures are useful for non-destructive test. We have shown, qualitatively, the effects of surface defects on the resonance spectrum of the balls. We can conclude our observations as (1) decrease in Q, (2) overall decrease in surface resonance peak amplitude, (3) scrambling effect at high frequencies ($k_R a \gtrsim 200$), and (4) increase in the apparent surface wave velocity. The second and third phenomena will probably take too long to finish in one experiment, while the first and fourth phenomena seem to be the faster ways to observe the existence of surface defects. For the first phenomenon, we recall the measurement of Q requires curve fitting phase information near resonance using equation:

$$\theta = \theta_0 - tan^{-1} \frac{\left(f^2 - f_0^2\right)Q}{f f_0} \tag{16}$$

Where θ_0 is the phase at resonance, f_0 is the resonance frequency at each point and Q is the quality factor.

For the fourth phenomenon, we use equation (15) to find the apparent surface wave velocity. It is necessary to be able to predict surface wave resonance frequencies in order to speed up the measurement. To do this, we have to be able to accurately calculate material properties V_l and V_s in advance. In section A.3.3, we will discuss the dispersion of surface waves on a sphere. By using V_l and V_s calculated from the low frequency measurement, we can predict each one of the high frequency surface resonance modes and verify with high frequency measurements. In section A.3.4, we will discuss the dependence of acoustic velocities with temperature. It is useful to establish this dependence relationship to calibrate for high frequency measurement.

A.3.3 Dispersion of Surface Waves on a Sphere

We demonstrate in this section the capability of the one-point-contact technique on small bearing balls. We measured, from 100 KHz to 70 MHz, the resonance spectrum of a good Si_3N_4 bearing ball with a diameter of 1mm. As discussed before, in the low frequency spectrum, we can identify resonant frequencies of bulk resonant modes. We see that this technique, unlike the contact technique, excites only spheroidal modes. This is because there is only one point of contact, and the excitation

42

direction is in the normal direction of the contact. It also
helps to explain the alignment difficulty for the contact-contact
technique where we observed torsional modes. We chose two high
Q spheroidal modes to calculate material properties of the 1mm
diameter sphere using equation (17), A purely torsional case
where the radial component of Ψ is equal to zero and the
displacement vector is given by:

$$\left.\begin{aligned}
u_{r,3} &= 0 \\
u_{\theta,3} &= \frac{mC_{mn}}{n(n+1))} \frac{J_{n+1/2}(k_s r)}{r^{1/2}} \frac{P_n^m(\cos\theta)}{\sin\theta} \cos(m\phi) \\
u_{\phi,3} &= -\frac{C_{mn}}{n(n+1)} \frac{J_{n+1/2}(k_s r)}{r^{1/2}} \frac{d}{d\theta} P_n^m(\cos\theta) \sin(m\phi)
\end{aligned}\right\} \qquad (17)$$

In equation (17), the subscript 3 stands for the solution to
Ψ with no radial component. The results are shown in Table A-1.
The calculated values of V_l and V_s were then used to calculate the
dispersion curve of surface waves using equation (17). For each
positive integer n, the first solution to equation (17) is mode
S_{n0} , which corresponds to surface wave resonance mode (there is
no surface wave resonance mode solution for $n = 1$). For n larger
than 100, the equation asymptotically approaches that of the
Rayleigh wave characteristic as shown in equation (18):

$$\frac{V_R}{V_s} = 0.87379 + 0.20178\nu - 0.077453\nu^2 \qquad (18)$$

Table A-1
Material properties of a ceramic bearing ball with a diameter of
1.0 mm, calculated from two high Q spheroidal modes.

ν (Poisson's Ratio)	V_l (m/s)	V_s (m/s)	V_R (m/s)
0.26646	10999	6206.1	5772.6

The calculated surface wave dispersion curve is then compared to the experimentally measured surface wave resonances, as seen in Figure A-13. The theoretical prediction and measurement agree with each other very well. Each one of the surface wave modes is predicted and measured. This means if we know V_l and V_s accurately, we should be able to predict where the high frequency resonance modes are. We also see that the apparent surface wave velocity asymptotically approaches a constant-true Rayleigh wave velocity. As shown in Figure A-14, V_R starts approaching a constant when $k_R a \geq 40$.
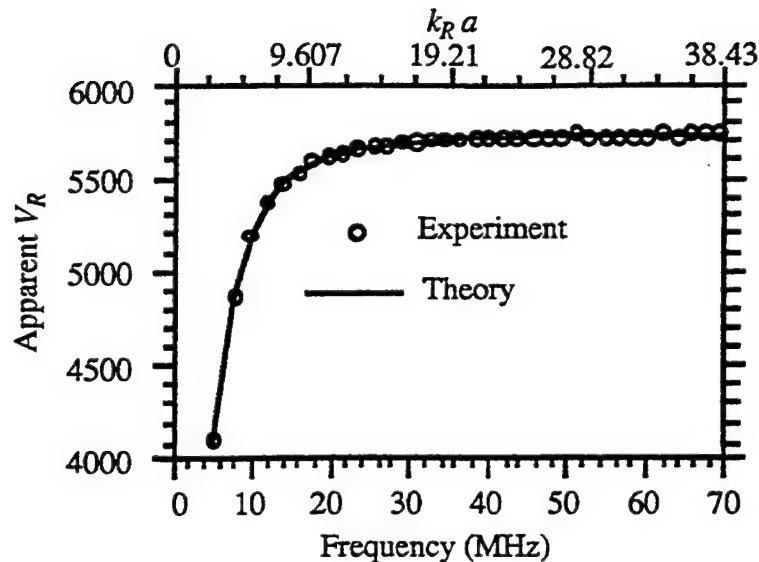

Figure A-14 Dispersion Relation of surface waves on a sphere.

A.3.4   Temperature Calibration

In section A.3.2 we discussed the necessity to get accurate numbers for Vl and Vs. In this section, the optical probing technique is used to observe the change in acoustic velocities with respect to temperature variation. Figure A-15 illustrates the temperature changes in the laboratory within a 42-hour time period.
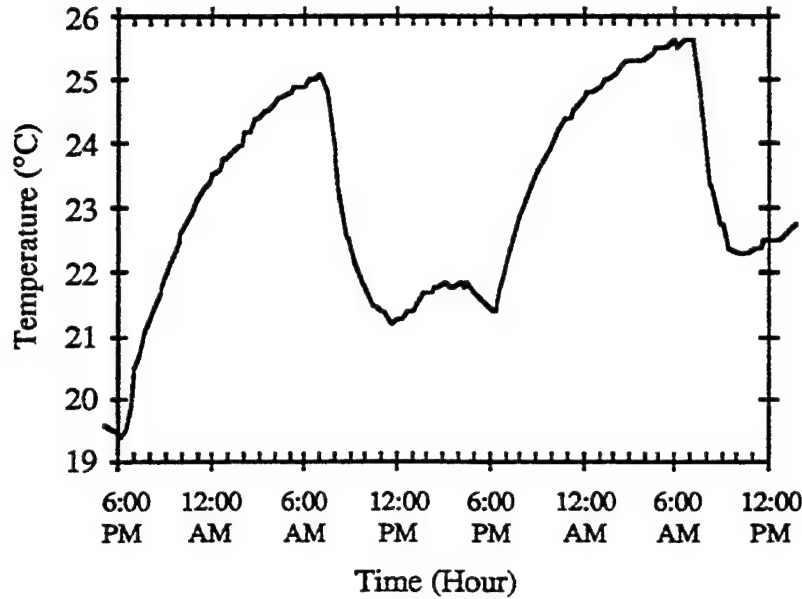
Figure A-15 Temperature changes in the laboratory.

For a laboratory temperature variation between 19°C and 26°C, we continuously measured two high Q spheriodial modes. We then used these two modes to calculate V_s and V_l. Figures A-16 and A-17 show the calculated velocity-temperature relationship. In Figure A-16.

$$\begin{cases} V_l = 11177 - 0.15524T \\ \dfrac{1}{V_l}\dfrac{dV_l}{dT} = -1.38892 \cdot 10^{-5} - 1.92911 \cdot 10^{-10}T \end{cases} \qquad (19)$$

and from Figure A-17,

$$\begin{cases} V_s = 6322.8 - 0.087853T \\ \dfrac{1}{V_s}\dfrac{dV_s}{dT} = -1.38946 \cdot 10^{-5} - 1.93061 \cdot 10^{-10}T^{\cdot} \end{cases} \qquad (20)$$

45

$$s^2 = k_R^2 - k_s^2 \qquad (21)$$

Combining equations (19), (20) and (21) into equation (22), it can be shown that Poisson's ratio is:

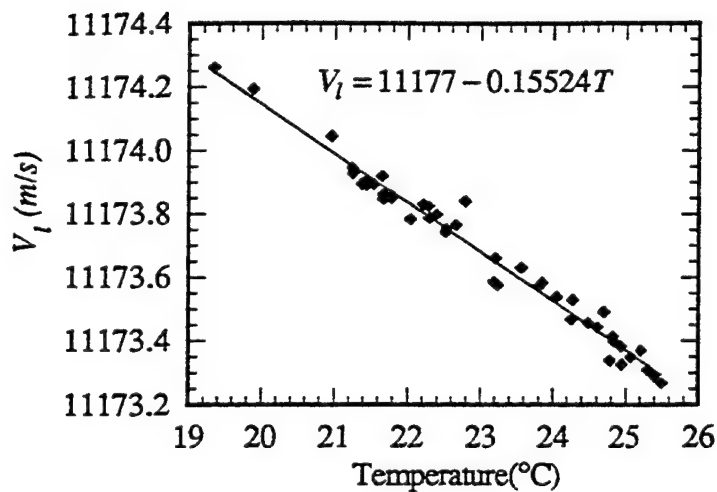$$\nu = 0.264691 + 3.73871 \times 10^{-9}\,T. \qquad (22)$$

Figure A-16 Longitudinal wave velocity change versus laboratory temperature change for Si_3N_4 material
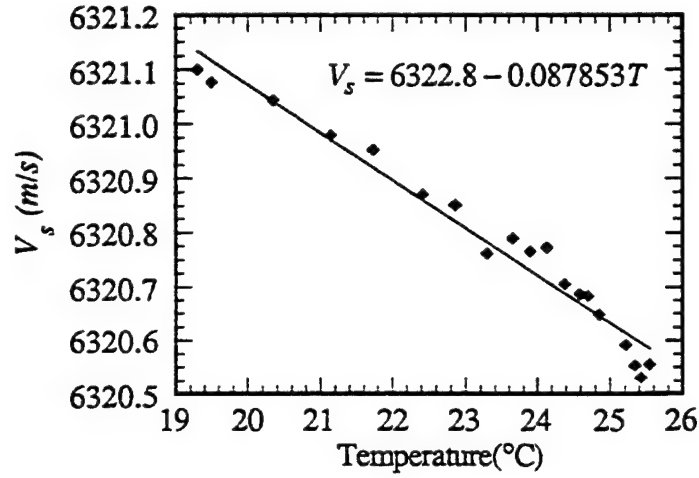
Figure A-17 Shear wave velocity change versus laboratory
temperature change for Si_3N_4 material.

Also, combining equations (19), (20) and (23) into equation (24),
it can be shown that the Rayleigh wave velocity is:

$$
\begin{bmatrix} \sigma_{xx} \\ \sigma_{yy} \\ \sigma_{zz} \\ \sigma_{yz} \\ \sigma_{xz} \\ \sigma_{xy} \end{bmatrix} = \begin{bmatrix} \lambda+2\mu & \lambda & \lambda & 0 & 0 & 0 \\ \lambda & \lambda+2\mu & \lambda & 0 & 0 & 0 \\ \lambda & \lambda & \lambda+2\mu & 0 & 0 & 0 \\ 0 & 0 & 0 & \mu & 0 & 0 \\ 0 & 0 & 0 & 0 & \mu & 0 \\ 0 & 0 & 0 & 0 & 0 & \mu \end{bmatrix} \begin{bmatrix} \partial u_x/\partial x \\ \partial u_y/\partial y \\ \partial u_z/\partial z \\ \left(\partial u_y/\partial z\right)+\left(\partial u_z/\partial y\right) \\ \left(\partial u_x/\partial z\right)+\left(\partial u_z/\partial x\right) \\ \left(\partial u_x/\partial y\right)+\left(\partial u_y/\partial x\right) \end{bmatrix} \qquad (23)
$$

$$
V_R = 5828.18 - 0.0809767T. \qquad (24)
$$

47

Equations (19), (20) and (24) all show a decrease in acoustic velocity with an increase in temperature. This phenomenon can be explained by the following physical interpretation. Acoustic velocity is equal to the square root of stiffness divided by density. As temperature increases, the material becomes softer and the stiffness decreases, also, the density decreases due to thermal expansion. Therefore, as temperature increases, the acoustic velocity decreases. The ordinates of Figure A-16 and A-17 also show the high degree of accuracy in our measurement.

The above argument is verified by calculating the dependence of stiffness constants $c_{11}=\lambda+2\mu$ and $c_{44}=\mu$ where λ and μ are the Lam´e constants[29]. The theoretical value for density of Si_3N_4 ceramic material is 3270 Kg/m^3. Combining equations (19), (20) and

$$\begin{cases} V_l = \sqrt{\dfrac{c_{11}}{\rho}} \\ Vs = \sqrt{\dfrac{c_{44}}{\rho}} \end{cases}, \qquad (25)$$

we get

$$\begin{cases} \dfrac{dc_{11}}{dT} = -1.13477 \cdot 10^7 + 157.610T \\ \dfrac{dc_{44}}{dT} = -3.63282 \cdot 10^6 + 50.4767T \end{cases} \qquad (26)$$

48

A.4.0   CONCLUDING REMARKS

In this Appendix, we demonstrated a new technique capable of measuring the material properties of spherical objects and capable of inspecting them for the presence of surface defects. The technique uses a single point contact to excite resonance in the object and an optical interferometer to measure these resonances. The measurement can be made on spherical objects of any size and over an unlimited frequency range. We also showed, for the first time, good agreement between theory and experiment for the dispersion relation of surface waves on a sphere. This technique has the potential of inspecting nonmetallic spheres, or spheres with coatings and cylindrical objects. It may also be applied to objects of uncommon geometries.

Bibliography

[1] S.P. Timoshenko and J.N. Goodier, *Theory of Elasticity*, 3rd Edition, McGraw-Hill Book Company (1970).

[2] D. Royer, E. Dieulesaint, X. Jia and Y. Shui, *Optical Generation and Detection of Surface Acoustic Waves on a Sphere*, Appl. Phys. Lett **52**(17)(1988).

[3] Dr. Chris Scrub, Manager, Manufacturing NDT, The National NDT Centre, Harwell Laboratory, Oxfordshire OX11 ORA, private communication.

[4] Jean-Pierre Monchalin, *Optical Detection of Ultrasound*, in *IEEE Transactions on Ultrasonics, Ferroelectrics, and Frequency Control*, **UFFC-33**, No. 5, (September 1986).

[5] G.I. Stegeman, *Optical Probing of Surface Waves and Surface Wave Devices.* IEEE Trans. Sonics Ultrason., **SU-23** (1976).

[6] R. Adler, A Korpel and P. Desmares, *An Instrument for Making Surface Waves Visible*, IEEE Trans. Sonics. Ultrason., SU-15 (1967).

[7] G. Alers, M.A. Tennison, R.B. Thompson and B.R. Tittmann, *Visualization of Surface Elastic Waves on Structural Materials*, Ultrasonics, **11**, (1973).

[8] H. Engan, *Phase Sensitive Laser Probe for High-Frequency Surface Acoustic Wave Measurements*, IEEE Trans. Sonics. Ultrason., **SU-25**, (1978).

[9] H. Sontag and A.C. Tam, *Optical Detection of Nanosecond Acoustic Pulses*, IEEE Trans. Ultrason., Ferroelectrics, Freq Contr. **UFFC-33**, (5), (1986).

[10] M. A. Olmstead and N. M. Amer, *A New Probe of the Optical Properties of Surfaces*, J. Vac. Sci. Technol, **B1** (1983).

[11] J. Opsal, A. Rosencwaig and D.L. Willenborg, *Thermal-Wave Detection and Thin-Film Thickness Measurements with Laser Beam Deflection*, App. Opt. 22, (1983).

[12] G.I. Stegeman, *Optical Probing of Surface Waves and Surface Wave Devices*. IEEE Trans. Sonics Ultrason., **SU-23** (1976).

[13] R.L. Whitman and A. Korpel, *Probing of Acoustic Surface Perturbations by Coherent Light*, App. Opt. 8, (1969).

[14] C. Thomsen, H.T. Grahn, H.J. Maris and J. Taue, *Ultrasonic Measurement with Picosecond Time Resolution*, J. Physique, Colloque C10, suppl, **46** (1985).

[15] Wolf Bickel, *Method and Apparatus for Receiving Ultrasonic Waves by Optical Means*, U.S. Patent #4,129,041, Dec. 1978, assigned to Krautkrämer-Branson Inc.

[16] Wolf Bickel, *Method and Apparatus for Receiving Ultrasonic Waves by Optical Means*, U.S. Patent #4,129,041, Dec. 1978, assigned to Krautkrämer-Branson Inc.

[17] Wolf Bickel, *Method and Apparatus for Receiving Ultrasonic Waves by Optical Means*, U.S. Patent #4,345,475, Aug. 1982, assigned to Krautkrämer-Branson Inc.

[18] G.A. Massey and R.R. Carter, *Portable Laser Instrument for Vibration Analysis and Transducer Calibration*, Shock and Vibration Bull. 37, Part 2, (1968).

[19] P. Buchhave, *Laser Doppler Vibration Measurements Using Variable Frequency Shift*, DISA Informat., no.18, (1975).

[20] G. Bouchard and D.B. Bogy, *Experimental Measurement of Scattered Surface Waves Using a Laser-Doppler Technique*, J. Acoust. Soc. Amer, 77, (1985).

[21] J.P. Monchalin, Optical Detection of Ultrasound at a Distance, Can. J. Soc. Nondestructive Testing, **6**, (1984).

[22] R.L. Whitman, L.J. Laub and W.Bates, Acoustic Surface Displacement Measurements on a Wedge-Shaped Transducer Using an Optical Probe Technique, IEEE Trans. Sonics Ultrason. **SU-15**, (1968).

[23] R. Dändliker and J.F. Willemin, *Measuring Microvibrations by Heterodyne Speckle Interferometry*, Optics Lett. **6**, (1981).

[24] C.H. Palmer and R. O. Claus, *Application of Optical Fibers to Wideband Differential Interferometry*, Mat. Eval, **41**, (1983).

[25] L.M. Barker, *Laser Interferometry in Shock-Wave Research*, Exp. Mech., (May, 1972).

[26] W. Kaule, *Interferometric Method and Apparatus for Sensing Surface Deformation of a Workpiece Subjected to Acoustic Energy*, US patent #4,046,477, Sept. 1977, assigned to Krautkrämer-Branson Inc.

[27] D. Royer and E. Dieulesaint, *Optical Probing of the Mechanical Impulse Response of a Transducer*, Appl. Phys. Lett. **49** (17) (1986).

[28] G.S. Kino, *Acoustic Waves: Devices, Imaging and Analog Signal Processing* Prentice-Hall, New Jersey, (1987).

[29] B. A. Auld, *Acoustic Fields and Waves in Solids*, Vol. 1, 2nd ed., Robert E. Krieger Publishing Company, Malabar, Florida, (1990).